Chemical Geology 615 (2023) 121213

Contents lists available at ScienceDirect

Chemical Geology

journal homepage: www.elsevier.com/locate/chemgeo

NanoSIMS as an analytical tool for measuring oxygen and hydrogen isotopes in clay minerals from palaeosols: Analytical procedure and preliminary results

Elisa Laita [a,*], Maria Angels Subirana [b], Dirk Schaumlöffel [b], Alfonso Yuste [a], Blanca Bauluz [a]

[a] IUCA-Department of Earth Sciences, Faculty of Sciences, University of Zaragoza, Pedro Cerbuna 12, 50009 Zaragoza, Spain
[b] CNRS, Université de Pau et des Pays de l'Adour, E2S UPPA, Institut des Sciences Analytiques et de Physico-Chimie pour l'Environnement et les Matériaux (IPREM), UMR 5254, 64000 Pau, France

ARTICLE INFO

Editor: Karen Johannesson

Keywords:
Hydrogen isotopes
Kaolinite
NanoSIMS
Oxygen isotopes
Smectite

ABSTRACT

Oxygen and hydrogen isotope composition of neoformed clay minerals is commonly used as a palaeoclimatic proxy. Usually, sediments and rocks (including palaeosols) contain not only neoformed clay minerals, but also detrital and/or diagenetic ones. Together with the usually small size (micro- or nanometric) of the clay minerals in these materials, this can generate difficulties during isotopic analyses by conventional spectrometry. To avoid this problem, we used nanoscale secondary ion mass spectrometry (NanoSIMS) to analyse neoformed clay minerals included in palaeosol levels in early Barremian continental profiles located in NE Spain. The bottom levels of the profiles are rich in kaolinite, whereas the top levels contain smectite (beidellite-type). The isotopic compositions of pure powder standards of kaolinite and beidellite were measured in bulk by conventional mass spectrometry to obtain reference values for calibrating the instrumental mass fractionation. Two common preparation techniques for geological samples were tested (thin sections and thick polished sections), revealing that thin sections are more suitable for NanoSIMS analysis due to their lower resin content. The high spatial resolution of the instrument allowed the elemental mapping of the samples, permitting the localization of the minerals of interest and the measurement of isotopic ratios at selected points (1 x 1 μm^2) within the samples. The preliminary isotopic results allowed to distinguish a decrease in the average $^{18}O/^{16}O$ and D/H ratios from the kaolinite in the bottom levels to the smectite in the top levels, reflecting a change in the climatic conditions. The average $\delta^{18}O$ and δD values obtained for kaolinite ($\delta^{18}O_{SMOW}$=18±15‰; δD_{SMOW}=-82±36‰ and $\delta^{18}O_{SMOW}$=14 ±4‰; δD_{SMOW}=-97±37‰) and smectite ($\delta^{18}O_{SMOW}$=13±14‰; δD_{SMOW}=-167±87‰ and $\delta^{18}O_{SMOW}$=11±6‰; δD_{SMOW}=-180±40‰;), respectively, are consistent with the crystallization of the clays in weathering conditions. Despite the uncertainties of these preliminary isotopic measures, the results obtained allowed to estimate an average temperature for kaolinite formation of 21-22°C, and of 16-17°C for smectite. Given suitable calibration using pure isotopic standards and adequate sample preparation, NanoSIMS can thus have a great applicability in palaeoclimatic studies involving the oxygen and hydrogen isotopic composition of nanometre-sized clay minerals from palaeosols samples.

1. Introduction

NanoSIMS (nanoscale secondary ion mass spectrometry) is a dynamic SIMS technique that allows the mapping of different chemical elements at nanometre scale, with high sensitivity as well as high spatial resolution (Mosenfelder et al., 2011; Blanc et al., 2012; Subirana et al., 2021).

The focus of the primary ion beam perpendicular to the sample surface allows the high spatial resolution achieved by NanoSIMS, combining with high-sensitive chemical and isotopic images (Subirana et al., 2021). The primary ion bean of NanoSIMS can be positive (Cs^+) or negative (O^-), in order to generate respectively either negative or positive secondary ions from the sample surface and obtain the corresponding elemental images. The positive Cs^+ ion beam can achieve 50 nm resolution images of electronegative elements such as oxygen, silicon, carbon and hydrogen. On the other hand, the rf (radio frequency)

* Corresponding author.
E-mail address: laita@unizar.es (E. Laita).

https://doi.org/10.1016/j.chemgeo.2022.121213
Received 26 April 2022; Received in revised form 27 September 2022; Accepted 9 November 2022
Available online 15 November 2022

plasma O^- ion beam allows high lateral resolution imaging below 40 nm of electropositive elements, such as most metals (Malherbe et al., 2016; Agüi-Gonzalez et al., 2019; Subirana et al., 2021). In addition, the NanoSIMS instrument is equipped with a charged-coupled device (CCD) camera, which allows optical imaging and thus the preselection of regions of the sample of interest for subsequent SIMS analysis (Chew et al., 2014; Ender et al., 2019).

These characteristics make NanoSIMS suitable for investigating heterogeneous materials, since it allows the mapping and stable isotopic analyses of nanometric phases. In this way, NanoSIMS has been applied to several geological materials to achieve sub-micron scale imaging and *in-situ* isotope ratio analysis. For example, Wacey et al. (2008) described a biological origin of ambient inclusion tails (AIT) through elemental images of C, N, P, S, Co, Fe, Ni and Zn, together with $^{13}C/^{12}C$ isotope ratios analysis. Hu et al. (2014) measured D/H ratios in melt inclusions and apatite in a Martian meteorite. Other examples of NanoSIMS applications in the Geosciences are reported in Kilburn and Wacey (2015), (e.g., $^{56}Fe^{16}O^-$ and $^{12}C^{14}N^-$ maps in iron oxides concretions or variations in $^{24}Mg^-/^{44}Ca$ ratios in foraminifera).

There are also investigations that use the NanoSIMS for elemental mapping of certain elements (e.g., C, N, Ca, Fe, Mn, Al, O, Cu) in soil samples (Mueller et al., 2012; Vogel et al., 2014; Rennert et al., 2014; Boiteau et al., 2020; Inagaki et al., 2020; Li et al., 2020; Vidal et al., 2020). Some of these studies report 40 x 40 μm^2 maps of the ions $^{16}O^-$, $^{12}C^-$, $^{13}C^-$, $^{12}C^{14}N^-$, $^{27}Al^{16}O$, $^{56}Fe^{16}O$ in the clay mineral fraction of the soils (Vogel et al., 2014; Inagaki et al., 2020).

As yet, however, there have been no investigations into the usefulness of NanoSIMS in palaeoclimatic studies involving the analysis of the O and H isotopic composition of the different neoformed nanometre-sized clay minerals that constitute de matrix of the past soils (i.e., palaeosols).

The isotopic composition of kaolinite and smectite can give useful information about their origin during palaeosol formation, since equilibrium isotopic fractionation factors are a function of temperature (Delgado and Reyes, 1996; Fernández-Caliani et al., 2010).

Measurement of the $^{18}O/^{16}O$ ratios of the structural oxygen in clay minerals is usually combined with D/H ratio analysis, since they both provide information about the formation conditions of these minerals (Savin and Hsieh, 1998; Sheppard and Gilg, 1996; Sheldon and Tabor, 2009; Kuligiewicz et al., 2021).

Under warm and humid conditions (subtropical to tropical), very effective hydrolysis is produced by intense chemical weathering, giving rise to the formation of oxisols. In oxisols (commonly known as laterites), the main clay mineral is kaolinite, along with aluminium and iron oxides, oxyhydroxides and hydroxides (e.g., Mack et al., 1993; Do Campo et al., 2018; Laita et al., 2020; Laita et al., 2022). In contrast, under drier and colder conditions there is an absence of significant hydrolysis, enhancing the formation of smectite and illite (Dhillon and Dhillon, 1991; Do Campo et al., 2018; Laita et al., 2022).

During lateritic weathering, kaolinite, and iron oxides/oxyhydroxides are formed in isotopic equilibrium with the meteoric water (Bird et al., 1992; Girard et al., 2000, 2002). However, the presence of other silicates with a different provenance, such as detrital quartz or micas, in palaeosols may create problems in isotopic investigations since they are not in isotopic equilibrium with the minerals formed during weathering (Kuligiewicz et al., 2021).

Traditional isotope ratio mass spectrometry (IRMS) is commonly used for $\delta^{18}O$ and δD measurements of clay separates in bulk (e.g., Fernández-Caliani et al., 2010; Mix and Chamberlain, 2014; Clauer et al., 2015).

For this kind of studies, the bulk powder samples are centrifugated to obtain fine fractions (0.5-2 μm) to isolate the clay minerals. However, even in these fractions there can be a great variety of clay mineral assemblages of different origin. In other studies, the mineral of interest is separated from the rest of the phases by applying specific chemical treatments to the sample (e.g., Delgado and Reyes, 1996; Giral-Kacmarcík et al., 1998; Gilg et al., 2003; Gilg et al., 2004).

Although these sample treatments can reduce the problem of analysing the isotopic signal of mixed phases, there is no reliable way to ensure that the clay mineral of interest is isolated from the sample. This fact, along with the small particle size of the clay minerals (from micrometric to nanometric), leads to difficulties during isotopic analysis of these minerals by conventional spectrometry (Tabor et al., 2002; Kuligiewicz et al., 2021). These difficulties have been reported in other geological materials (e.g., chondrites), where the mixture of organic matter and hydrous silicates hinders the individual determination of D/H ratios (Piani et al., 2012; Piani et al., 2015).

The use of NanoSIMS for the isotopic study of clay minerals included in palaeosols during weathering could solve this problem, since the high spatial resolution of the technique allows to select zones enriched in one single small-sized neoformed clay mineral in polished paleosols samples and thus, to analyse its isotopic composition separately, without interference from other minerals included in the sample.

In this research, therefore, we carried out $^{18}O/^{16}O$ and D/H isotopic analysis of the neoformed clay minerals (kaolinite and beidellite) included in Lower Cretaceous (early Barremian) lateritic palaeosols from NE Spain with two aims: 1) to evaluate the applicability of NanoSIMS in palaeoclimatic research using O and H isotopic values of neoformed clay minerals included in palaeosols samples, since there is to date no published research in this topic, and 2) to obtain preliminary results that help to deduce the climatic conditions under which these materials were generated.

2. Palaeosols samples description

The samples are from palaeosol levels included in early Barremian (Early Cretaceous ~129–128 million years) continental profiles from the Iberian Range (NE Spain). Laita et al. (2020) characterised these materials through a combined facies and clay mineral study by X-ray diffraction (XRD), optical and field emission scanning electron microscopy (FESEM) and energy-dispersive X-ray (EDS) analyses. The facies analyses of these continental successions revealed that the paleosols levels developed *in-situ* by the chemical weathering of lacustrine marlstones. According to the XRD patterns and the EDS analyses the palaeosol levels are mainly formed by clay minerals (kaolinite, beidellite-type smectite and illitic phases), together with Fe and Ti oxides and oxyhydroxides (goethite, hematite, anatase, rutile, ilmenite, and diaspore), quartz and calcite nodules (Figure 1a-c) (Laita et al., 2020).

The textural data reported by Laita et al. (2020) indicate that kaolinite and smectite are neoformed and crystallized during the soil development. FESEM images showing kaolinite books and smectite with flake-type morphologies forming the matrix of the paleosols together with the Fe and Ti oxides and oxyhydroxides discard a detrital origin of these minerals (Figure 2a-c). On the other hand, the anhedral morphologies of the illitic phases (Figure 2d), along with the fact that the formation of illite is not compatible with that of the kaolinite in these environments, suggest a detrital origin for the illitic phases (Bauluz et al., 2014; Laita et al., 2020). The mineral assemblage that forms the palaeosols, along with the presence of the ferruginous pisoids allowed Laita et al. (2020) to classify them as laterites.

Laita et al. (2020) described a decrease in the neoformed kaolinite content towards the top of the profiles that coincided with an increase in neoformed smectite and detrital illitic phases content, which reflected a decrease in the chemical weathering intensity related with a change from warm/humid to colder/drier conditions.

Due the aforementioned reasons, samples from two profiles of those described by Laita et al. (2020) (ALC and JO) were selected for the NanoSIMS study. Samples were chosen due to their high content in neoformed kaolinite and smectite, whose isotopic composition can yield information about the palaeoenvironment and palaeotemperature in which they were generated. Three samples correspond to lower, middle and upper palaeosol levels from the ALC profile (samples ALC-1, ALC-4

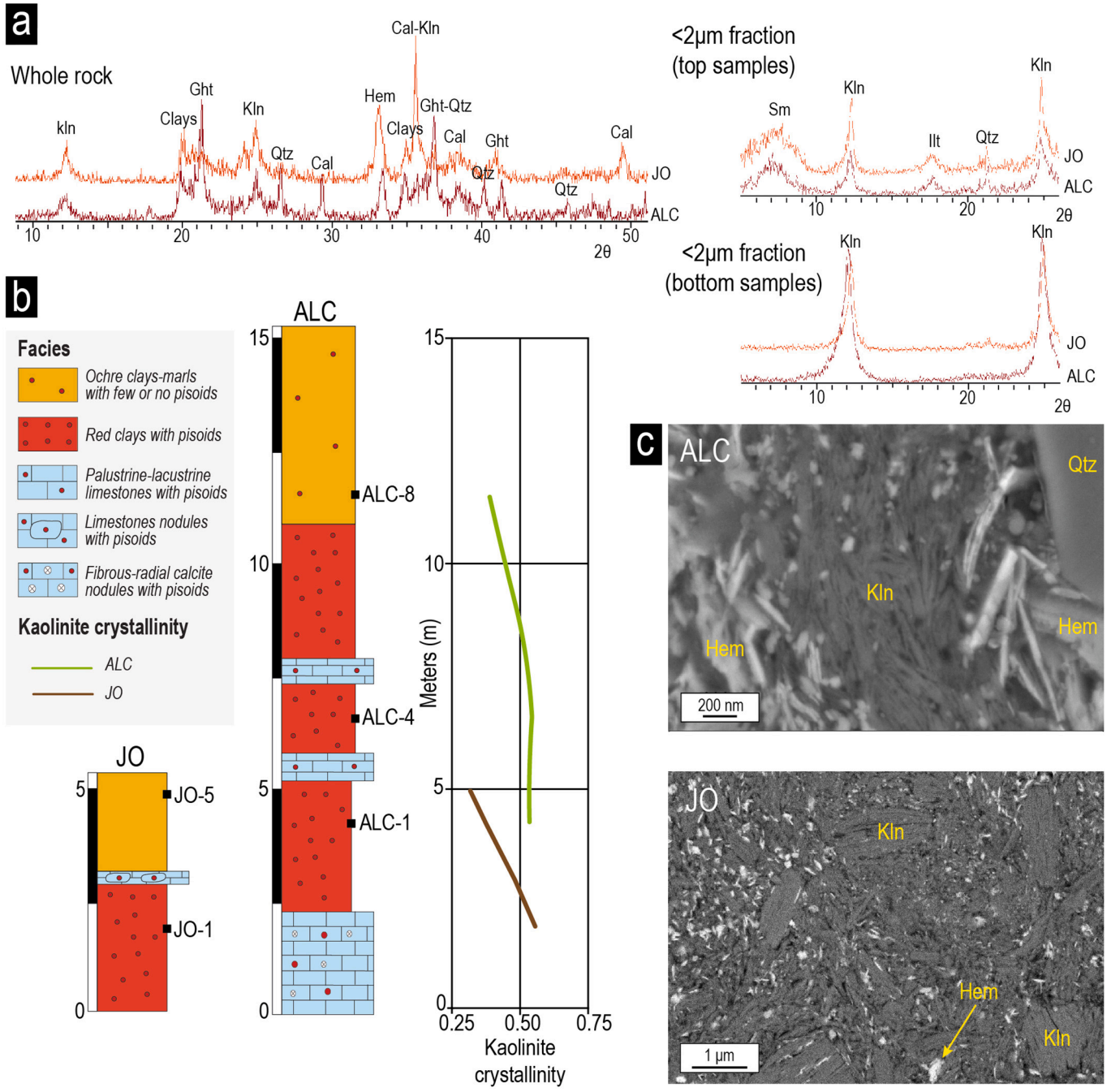

Fig. 1. a) XRD patters of the whole rock and < 2μm fractions of palaeosols samples from the ALC and JO profiles; b) Location of the samples under study in the Lower Barremian ALC (ALC-1, ALC-4 and ALC-8) and JO (JO-1 and JO-5) stratigraphic logs and kaolinite crystallinity values measured in these samples, with an average value of 0.5 and 0.4 for kaolinites from the ALC and JO samples, respectively; c) Backscattered electron images from the matrix of palaeosols samples from both profiles showing kaolinite plates and booklets. Clays=clay minerals, Ght=goethite, Qtz=quartz, Cal=calcite, Hem=hematite, Kln=kaolinite, Sm=smectite, Ilt=illitic phases. (Modified from Laita et al., 2020)

and ALC-8, respectively), and two other samples correspond to lower and upper palaeosol levels from the JO profile (samples JO-1 and JO-5, respectively), which are laterally equivalent to those of the ALC profile (Figure 1b). The samples from the lower and middle palaeosol levels (ALC-1, ALC-4, and JO-1) are rich in neoformed kaolinite, whereas the samples from the upper levels (ALC-8 and JO-5) contain neoformed smectite (Figure 1a and c).

3. Experimental section

3.1. Preparation of palaeosols for analysis

The samples were prepared for analysis by NanoSIMS in order to evaluate the potential of this technique for analysing areas rich in these minerals and determining their isotopic composition.

Thin sections were prepared from the five samples and studied using a Carl Zeiss Merlin field emission scanning electron microscope (FESEM) equipped with an Oxford energy-dispersive X-ray (EDS) detector at the University of Zaragoza (Zaragoza, Spain). The purpose of the FESEM

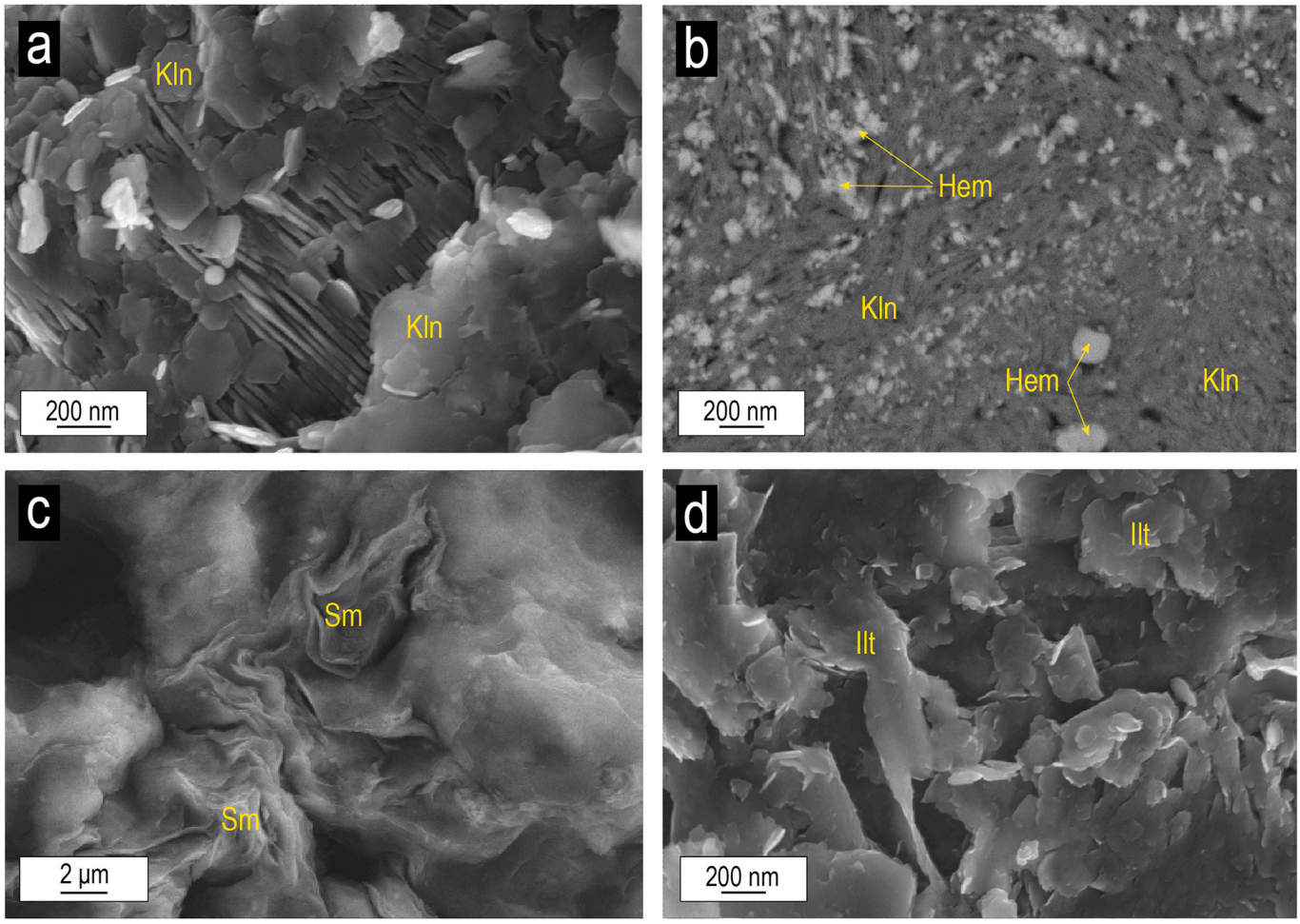

Fig. 2. Backscattered and secondary electron images of the matrix of palaeosol samples from the ALC and JO profiles showing: a) and b) kaolinite book-type aggregates and platy kaolinites displaying pseudohexagonal outlines; c) smectite with flake-type morphologies and d) anhedral illitic phases. Kln=kaolinite, Hem=hematite, Sm=smectite, Ilt=illitic phases. (Modified from Laita et al., 2020).

imaging was to find areas in each sample enriched in the neoformed clay minerals suitable for isotopic analysis.

On the other hand, palaeosol samples can occasionally be poorly consolidated, leading to problems with the polishing of sections, since the surface of the sample can undergo plucking and deformation (Camuti and McGuire, 1999). For this reason, thick polished sections of samples ALC-1 and ALC-4 embedded in epoxy resin were prepared in order to evaluate which method of sample preparation was better for carrying out the isotopic analysis of clay minerals by NanoSIMS.

The common geological thin sections (27 x 45 mm, 30 µm thick) are larger than the NanoSIMS sample holder (Ø = 25.4 mm), so they were cut smaller, and a custom metal sample holder was designed and manufactured in-house at the SIAME laboratory of the University of Pau and the Pays de l'Adour (France), so the thin sections would fit in the NanoSIMS sample holder and thus be positioned for analysis perpendicular to the primary ion beam.

The interlayer and absorbed water in clay minerals can exchange with the atmospheric water vapour within a few hours (Savin and Hsieh, 1998), and surface contamination can lead to a high background in the hydrogen measures (Hu et al., 2014). These factors could result in lower measured δD values (Bauer and Vennemann, 2014).

To minimize these problems, both the thin sections and the thick polished sections were heated at 150°C for at least 2h to remove the absorbed atmospheric water. Afterwards, they were coated with 5 nm of gold using a Cressington 108 Auto Sputter Coater (Cressington, Watford, UK) and rapidly placed inside the NanoSIMS under vacuum in order to prevent the reabsorption of water. Additionally, they were kept in the vacuum chamber of the equipment overnight before the oxygen analyses and for a week before the hydrogen analyses to ensure the removal of remaining gases and water that could be trapped within the sample. The resulting pressure in the analysis chamber during the sample analysis was $4x10^{-11}$ mbar, which is the same pressure that is achieved without any sample in the chamber.

3.2. Standard reference analysis

The isotopic compositions of pure powder standards of kaolinite and smectite were measured at the Nucleus Laboratory of the University of Salamanca (Spain) to obtain reference values. The smectite used as standard has a beidellite composition and was generated by hydrothermal alteration from volcanic rocks. The company Sepiolsa-Minersa mined these materials and supplied them. The kaolinite standard come from the Source Clays Repository (label Kaolin KGa-2). The purity of both standards was checked by XRD.

The isotopic analysis in the reference laboratory was carried out by using a SIRA-II and SIRA-10 spectrometers in dual-inlet gas source mode. For the oxygen analyses, a glass vacuum line directly associated with the dual-inlet SIRA-II was used. The sample was laser ablated with a CO_2 laser in the presence of a small amount of ClF_3. The obtained oxygen was purified in various traps on the line and converted into CO_2 by reaction with graphite heated by a platinum resistor that finally was introduced into the spectrometer where it was analysed.

Table 1
$\delta^{18}O$ and δD relative to SMOW for the standards reported by the reference laboratory and calculated oxygen and hydrogen ratios.

	Reference standards data			
	$^{18}O/^{16}O$ Ratio	$\delta^{18}O_{SMOW}$ (‰)	D/H Ratio	δD_{SMOW} (‰)
Kaolinite	$2.03x10^{-3}$	19.8	$1.48x10^{-4}$	-62.4
Smectite	$2.03x10^{-3}$	18.9	$1.45x10^{-4}$	-79.4

For the hydrogen analyses, the sample was melted on a glass vacuum line through a platinum crucible heated by an induction furnace. The water obtained during the hydrogen analysis process was reduced in a furnace at 850°C with depleted uranium and the hydrogen was concentrated in the sample bottle by a Toeppler pump. The bottle was introduced to the dual-inlet SIRA-10 spectrometer where it was analysed.

The problem with atmospheric water was solved by heating the samples overnight under vacuum to temperature of 125°C before taking them (evacuated and closed) to the working line. All the values were corrected using international and internal standards, analysing them several times every day until obtaining values within ±0.2‰ of their real values. The oxygen and hydrogen isotope compositions of the kaolinite and smectite standards given by the reference laboratory were reported in δ notation relative to SMOW (standard mean ocean water) (Table 1).

Following the equation given by Hoefs (1997):

$$\delta_{in}‰ = \left[\left(R_{(Sample)} - R_{(Standard)}\right)/R_{(Standard)}\right] \text{ x } 1000$$

where R represents the measured isotope ratio, and knowing the $\delta^{18}O_{SMOW}$ and δD_{SMOW} values of the kaolinite and smectite standards reported by the reference laboratory, the $^{18}O/^{16}O$ and D/H ratios of the standards can be calculated as follows:

$$^{18}O/^{16}O_s = \left[\left(\delta^{18}O_s \text{ x } ^{18}O/^{16}O_{SMOW}\right)/1000\right] + {}^{18}O/^{16}O_{SMOW}$$

$$D/H_s = \left[\left(\delta D_s \text{ x } D/H_{SMOW}\right)/1000\right] + D/H_{SMOW}$$

where s is the powder standard (kaolinite or smectite) and the SMOW is the standard mean ocean water: $^{18}O/^{16}O_{SMOW} = 1.99x10^{-3}$ and $D/H_{SMOW} = 1.58x10^{-4}$ (Craig, 1961).

3.3. NanoSIMS analysis of the standards

The oxygen and hydrogen isotopes of the kaolinite and smectite standards were then measured by a CAMECA NanoSIMS 50L at the IPREM (CNRS-UPPA, Pau, France), equipped with a Cs^+ ion source and seven parallel electron multiplier detectors.

The standards were treated in a similar way as the palaeosols samples. They were heated at 150°C for 2h to ensure that the absorbed atmospheric water was removed. Then, they were dispersed on a carbon tape, coated with 5 nm of gold and immediately introduced inside the NanoSIMS.

Two areas of 30 x 30 μm^2 were pre-sputtered with Cs^+ ions in order to optimize the secondary ion yield. In each area, several spots of 1 x 1 μm^2 were analysed, with 32 x 32 pixels and a measuring time of 132 μs/pixel, with a Cs^+ current of 2.0-5.0 pA, using an aperture diaphragm of 200 μm (D1-3) and entrance slit of 50 x 220 μm (ES-1). The use of an entrance slit allowed the optimization of mass resolution to 6000-8000 in order to resolve possible isotopic interferences. Each spot was measured 270 times, organized in 10 blocks of 27 measurements each, resulting in 1 minute of measurement per spot. The average was calculated and corrected for the electron multiplier yield and dead time and for the background collected during the analysis, to obtain the resulting isotopic ratio. In addition, a threshold was also applied during the detector calibration to supress the noise coming from the electron multipliers and the white noise from the electronics. Two different magnetic fields were used in order to analyse the selected isotopes, since the distance in mass between O and H prevents the positioning of the electron multiplier detectors in a configuration allowing all isotopes to be measured simultaneously. Firstly, a magnetic field allowing the separation of the $^{18}O/^{16}O$ isotopes was applied, and detectors 2 and 3 used to measure $^{16}O^-$ and $^{18}O^-$ respectively. Subsequently a magnetic field adequate for the separation of the D/H isotopes was used, and H^- and D^- measured in detectors 1 and 2 respectively. Under these conditions, an average of $3.58x10^7$ counts were collected on $^{16}O^-$, $7.31x10^4$ counts on $^{18}O^-$, $1.07x10^7$ counts on H^- and $1.80x10^3$ counts on D^- for each single measure.

The aging of the detectors was also adjusted at the start of each analysis session. The isotopic ratios obtained by NanoSIMS for the kaolinite and smectite standards in each analytical session can be found in Table 2.

The ratios obtained for the kaolinite and smectite standards, in comparison with the ratios determined at the reference laboratory, were used for calibrating the instrumental mass fractionation (IMF) in the O and H isotope compositions of the samples by applying the formulae $\alpha_{IMF} = (^{18}O/^{16}O_m)/(^{18}O/^{16}O_r)$, and $\alpha_{IMF} = (D/H_m)/(D/H_r)$, where m is the ratio measured by NanoSIMS and r is the ratio reported by the reference laboratory. The instrumental mass fractionation was calibrated with the standards in each session of analysis (Table 2).

3.4. NanoSIMS imaging of the palaeosols samples

Elemental images of the ions $^{12}C^-$, $^{16}O^-$, $^{18}O^-$, $^{28}Si^-$, $^{27}Al^{16}O^-$ and $^{56}Fe^{16}O^-$ were measured in preselected areas from thin sections. The cluster ions $^{27}Al^{16}O^-$ and $^{56}Fe^{16}O^-$ were used to enhance the secondary ion yield obtained for Al and Fe, in the form of negative secondary ions (an opposite polarity to the positive primary ion beam is required by the coaxial optics). Mass calibration was performed using the kaolinite and smectite standards.

Areas of 40 x 40 μm^2 were pre-sputtered with Cs^+ ions and analysed using a 2.0 pA primary ion current. They were measured with 256 x 256 pixels with a dwell time of 5 ms/pixel. Two planes were consecutively analysed and stacked to obtain the final image using the software WinImage (CAMECA).

The size of the primary ion beam was calculated by the knife-edge method (16-84% criterion) (Malherbe et al., 2016) in order to determine the spatial resolution achieved by this method.

3.5. NanoSIMS isotopic analysis in the palaeosols samples

After the image acquisition, isotopic measurements were taken at different selected points containing kaolinite or smectite within those areas. The same instrumental conditions as those used for the measurement of the standards were used; an entrance slit was also used to optimize the mass resolution to 6000-8000, and the aging of the detectors was likewise adjusted at the start of each analysis session. Two different magnetic fields were used to collect, firstly, the $^{18}O/^{16}O$ isotopic ratio and, subsequently, the D/H ratio in the same spots. The same analysis conditions were used for O and H measurements. However, slightly different conditions were used for the analysis of thin sections and thick polished sections.

In thin sections, oxygen and hydrogen analyses were carried out in kaolinites of the samples ALC-1, ALC-4 and JO-1 and smectites of the samples ALC-8 and JO-5. Spots of 1 x 1 μm^2 were analysed with 32 x 32 pixels and a dwell time of 132 μs/pixel and a 2.0 pA Cs^+ current, in 10 blocks of 27 measurements (1 min analysis time). The use of a small current as well as short measuring times were necessary due to the thinness of the sample, which was otherwise rapidly consumed.

Table 2
$^{18}O/^{16}O$ and D/H ratios obtained for the kaolinite and smectite standards during the different NanoSIMS analytical sessions and the α_{IMF} obtained for each ratio. Kln=kaolinite; Sm=smectite; SD=standard deviation.

	Session 1 (Kln)				Session 2 (Kln)				Session 3 (kln)		Session 4 (Sm)				Session 5 (Sm)		Session 6 (Kln)				Session 7 (Sm)			
	$^{18}O/^{16}O$	α_{IMF}	D/H	α_{IMF}	$^{18}O/^{16}O$	α_{IMF}	D/H	α_{IMF}	$^{18}O/^{16}O$	α_{IMF}	$^{18}O/^{16}O$	α_{IMF}	D/H	α_{IMF}	D/H	α_{IMF}	$^{18}O/^{16}O$	α_{IMF}	D/H	α_{IMF}	$^{18}O/^{16}O$	α_{IMF}	D/H	α_{IMF}
	$1.92x10^{-3}$	0.95	$1.67x10^{-4}$	1.13	$2.01x10^{-3}$	0.99	$1.47x10^{-4}$	0.99	$1.98x10^{-3}$	0.98	$1.92x10^{-3}$	0.95	$1.33x10^{-4}$	0.90	$1.51x10^{-4}$	1.02	$2.06x10^{-3}$	1.01	$1.20x10^{-4}$	0.81	$1.97x10^{-3}$	0.97	$1.34x10^{-4}$	0.92
	$1.98x10^{-3}$	0.97	$1.83x10^{-4}$	1.24	$1.98x10^{-3}$	0.98	$1.43x10^{-4}$	0.96	$1.97x10^{-3}$	0.97	$2.00x10^{-3}$	0.98	$1.11x10^{-4}$	0.75	$1.53x10^{-4}$	1.03	$1.98x10^{-3}$	0.97	$1.22x10^{-4}$	0.82	$2.04x10^{-3}$	1.01	$1.33x10^{-4}$	0.92
	$1.91x10^{-3}$	0.94	$1.71x10^{-4}$	1.15	$1.98x10^{-3}$	0.97	$1.45x10^{-4}$	0.98	$1.92x10^{-3}$	0.95	$1.97x10^{-3}$	0.97	$1.20x10^{-4}$	0.81	$1.35x10^{-4}$	0.91	$1.97x10^{-3}$	0.97	$1.25x10^{-4}$	0.84	$2.03x10^{-3}$	1.00	$1.22x10^{-4}$	0.84
	$1.95x10^{-3}$	0.96	$1.90x10^{-4}$	1.28	$2.22x10^{-3}$	1.09	$1.42x10^{-4}$	0.96	$1.94x10^{-3}$	0.95	$2.01x10^{-3}$	0.99	$1.12x10^{-4}$	0.76	$1.37x10^{-4}$	0.92	$2.01x10^{-3}$	0.99	$1.28x10^{-4}$	0.86	$2.05x10^{-3}$	1.01	$1.25x10^{-4}$	0.86
	$1.97x10^{-3}$	0.97	$1.86x10^{-4}$	1.26	$1.90x10^{-3}$	0.93	$1.48x10^{-4}$	1.00	$2.05x10^{-3}$	1.01	$2.05x10^{-3}$	1.01	$1.39x10^{-4}$	0.94	$1.47x10^{-4}$	0.99	$2.03x10^{-3}$	1.00	$1.27x10^{-4}$	0.86	$2.06x10^{-3}$	1.02	$1.56x10^{-4}$	1.07
	$1.96x10^{-3}$	0.97	$1.99x10^{-4}$	1.34	$2.06x10^{-3}$	1.01	$1.43x10^{-4}$	0.96	$2.02x10^{-3}$	0.99	$2.06x10^{-3}$	1.02	$1.60x10^{-4}$	1.08	$1.32x10^{-4}$	0.89	$2.02x10^{-3}$	0.99	$1.26x10^{-4}$	0.85	$2.07x10^{-3}$	1.02	$1.25x10^{-4}$	0.86
	$1.96x10^{-3}$	0.96	$1.92x10^{-4}$	1.30	$1.98x10^{-3}$	0.97	$1.46x10^{-4}$	0.98	$2.01x10^{-3}$	0.99	$2.05x10^{-3}$	1.01	$1.27x10^{-4}$	0.86	-	-	$2.02x10^{-3}$	0.99	$1.19x10^{-4}$	0.80	$2.07x10^{-3}$	1.02	$1.28x10^{-4}$	0.88
	$1.91x10^{-3}$	0.94	$1.52x10^{-4}$	1.03	$2.16x10^{-3}$	1.06	$1.43x10^{-4}$	0.97	$1.99x10^{-3}$	0.98	$2.09x10^{-3}$	1.03	$1.31x10^{-4}$	0.89	-	-	$1.99x10^{-3}$	0.98	$1.14x10^{-4}$	0.77	$2.08x10^{-3}$	1.02	$1.23x10^{-4}$	0.84
	$1.95x10^{-3}$	0.96	$1.86x10^{-4}$	1.26	$2.11x10^{-3}$	1.04	-	-	$1.93x10^{-3}$	0.95	$2.05x10^{-3}$	1.01	$9.46x10^{-5}$	0.64	-	-	$2.00x10^{-3}$	0.98	$1.16x10^{-4}$	0.79	$1.98x10^{-3}$	0.98	$1.23x10^{-4}$	0.85
	$1.96x10^{-3}$	0.97	$1.50x10^{-4}$	1.01	$1.89x10^{-3}$	0.93	-	-	$1.99x10^{-3}$	0.98	$2.09x10^{-3}$	1.03	$1.27x10^{-4}$	0.86	-	-	$2.05x10^{-3}$	1.01	$1.25x10^{-4}$	0.85	-	-	$1.22x10^{-4}$	0.84
	$1.91x10^{-3}$	0.94	$1.72x10^{-4}$	1.16	$2.04x10^{-3}$	1.00	-	-	$2.04x10^{-3}$	1.00	$2.09x10^{-3}$	1.03	$1.30x10^{-4}$	0.88	-	-	$2.05x10^{-3}$	1.01	$1.15x10^{-4}$	0.78	-	-	$1.24x10^{-4}$	0.85
	$1.94x10^{-3}$	0.95	$1.34x10^{-4}$	0.91	$1.83x10^{-3}$	0.90	-	-	$1.93x10^{-3}$	0.95	$2.09x10^{-3}$	1.03	$1.14x10^{-4}$	0.77	-	-	-	-	$1.19x10^{-4}$	0.81	-	-	$1.32x10^{-4}$	0.91
	$2.00x10^{-3}$	0.98	$1.39x10^{-4}$	0.94	$2.00x10^{-3}$	0.98	-	-	$1.93x10^{-3}$	0.95	$2.02x10^{-3}$	0.99	$1.24x10^{-4}$	0.84	-	-	-	-	$1.22x10^{-4}$	0.82	-	-	$1.37x10^{-4}$	0.94
	$2.04x10^{-3}$	1.00	$1.06x10^{-4}$	0.71	$1.99x10^{-3}$	0.98	-	-	$2.03x10^{-3}$	1.00	$1.98x10^{-3}$	0.97	$1.50x10^{-4}$	1.01	-	-	-	-	-	-	-	-	$1.41x10^{-4}$	0.97
	$1.98x10^{-3}$	0.97	$1.35x10^{-4}$	0.91	$2.09x10^{-3}$	1.03	-	-	$1.94x10^{-3}$	0.95	$1.96x10^{-3}$	0.96	$1.76x10^{-4}$	1.19	-	-	-	-	-	-	-	-	$1.28x10^{-4}$	0.88
	$2.03x10^{-3}$	1.00	$1.36x10^{-4}$	0.92	$2.04x10^{-3}$	1.00	-	-	$1.91x10^{-3}$	0.94	$1.95x10^{-3}$	0.96	$1.99x10^{-4}$	1.34	-	-	-	-	-	-	-	-	$1.23x10^{-4}$	0.85
	$2.00x10^{-3}$	0.98	$1.30x10^{-4}$	0.88	$2.03x10^{-3}$	1.00	-	-	-	-	$1.94x10^{-3}$	0.95	$1.57x10^{-4}$	1.06	-	-	-	-	-	-	-	-	-	-
	$2.02x10^{-3}$	0.99	$1.27x10^{-4}$	0.86	$2.04x10^{-3}$	1.00	-	-	-	-	$1.94x10^{-3}$	0.96	$1.40x10^{-4}$	0.94	-	-	-	-	-	-	-	-	-	-
	$2.04x10^{-3}$	1.00	$1.50x10^{-4}$	1.01	$1.91x10^{-3}$	0.94	-	-	-	-	$1.94x10^{-3}$	0.96	$2.18x10^{-4}$	1.47	-	-	-	-	-	-	-	-	-	-
	$2.00x10^{-3}$	0.98	$1.43x10^{-4}$	0.97	$2.05x10^{-3}$	1.01	-	-	-	-	$1.90x10^{-3}$	0.94	$1.45x10^{-4}$	0.98	-	-	-	-	-	-	-	-	-	-
	$2.02x10^{-3}$	0.99	$1.38x10^{-4}$	0.93	$1.97x10^{-3}$	0.97	-	-	-	-	$1.91x10^{-3}$	0.94	$1.70x10^{-4}$	1.15	-	-	-	-	-	-	-	-	-	-
	$2.02x10^{-3}$	0.99	$1.50x10^{-4}$	1.02	$1.98x10^{-3}$	0.97	-	-	-	-	$1.94x10^{-3}$	0.96	$2.18x10^{-4}$	1.47	-	-	-	-	-	-	-	-	-	-
	$2.00x10^{-3}$	0.98	$1.35x10^{-4}$	0.91	$1.97x10^{-3}$	0.97	-	-	-	-	$1.93x10^{-3}$	0.95	$1.74x10^{-4}$	1.18	-	-	-	-	-	-	-	-	-	-
	-	-	$1.41x10^{-4}$	0.95	$2.06x10^{-3}$	1.01	-	-	-	-	-	-	-	-	-	-	-	-	-	-	-	-	-	-
Average	$1.98x10^{-3}$	0.97	$1.55x10^{-4}$	1.04	$2.01x10^{-3}$	0.99	$1.44x10^{-4}$	0.98	$1.97x10^{-3}$	0.97	$2.00x10^{-3}$	0.98	$1.46x10^{-4}$	0.99	$1.42x10^{-4}$	0.96	$2.02x10^{-3}$	0.99	$1.21x10^{-4}$	0.82	$2.04x10^{-3}$	1.00	$1.30x10^{-4}$	0.89
SD	$\pm4.18x10^{-5}$	±0.02	$\pm2.49x10^{-5}$	±0.17	$\pm8.38x10^{-5}$	±0.04	$\pm2.52x10^{-6}$	±0.02	$\pm4.64x10^{-5}$	±0.02	$\pm6.40x10^{-5}$	±0.03	$\pm3.34x10^{-5}$	±0.23	$\pm9.09x10^{-5}$	±0.06	$\pm3.01x10^{-5}$	±0.01	$\pm4.52x10^{-6}$	±0.03	$\pm3.83x10^{-5}$	±0.02	$\pm9.13x10^{-6}$	±0.06

In thick polished sections, oxygen analyses were carried out in kaolinites from samples ALC-1 and ALC-4, and hydrogen analyses in kaolinites from ALC-1. In a similar manner to thin sections, spots of 1 x 1 μm^2 were measured with 32 x 32 pixels, in 10 blocks of 27 measurements. However, the use of thicker samples permitted the use of higher measuring times and beam current without consuming the sample, which resulted in a higher signal for the measured isotopes and thus better statistics. A measuring time of 244 μs/pixel was used (which corresponds to 1.5 min analysis time), with a Cs^+ current of 5.0 pA. This higher current and dwell time also helped compensate for the lower secondary ion yield caused by the deterioration of the pressure in the analysis chamber due to the degassing of the epoxy resin.

In all cases, the resulting isotopic ratio was corrected for the electron multiplier yield and dead time as well as the background collected during the analysis.

4. Results and discussion

4.1. NanoSIMS imaging

The optical imaging of the CCD camera of the NanoSIMS allowed to locate the preselected regions by FESEM in the thin sections. Then elemental images were obtained for the ions $^{16}O^-$, $^{18}O^-$, $^{28}Si^-$, $^{27}Al^{16}O^-$, $^{56}Fe^{16}O^-$ and $^{12}C^-$ in these regions by analysing areas of 40 x 40μm^2 (Figure 3).

According to the knife-edge method (16-84% criterion) (Malherbe et al., 2016), the probe size during the images acquisition was 70 nm, which allowed the separation of the different nanoscale mineral components present on the selected area. The visualisation of these different elements facilitated the identification of pure zones of kaolinite and smectite for the following isotopic analyses, and the exclusion of iron oxides and oxyhydroxides and other silicates.

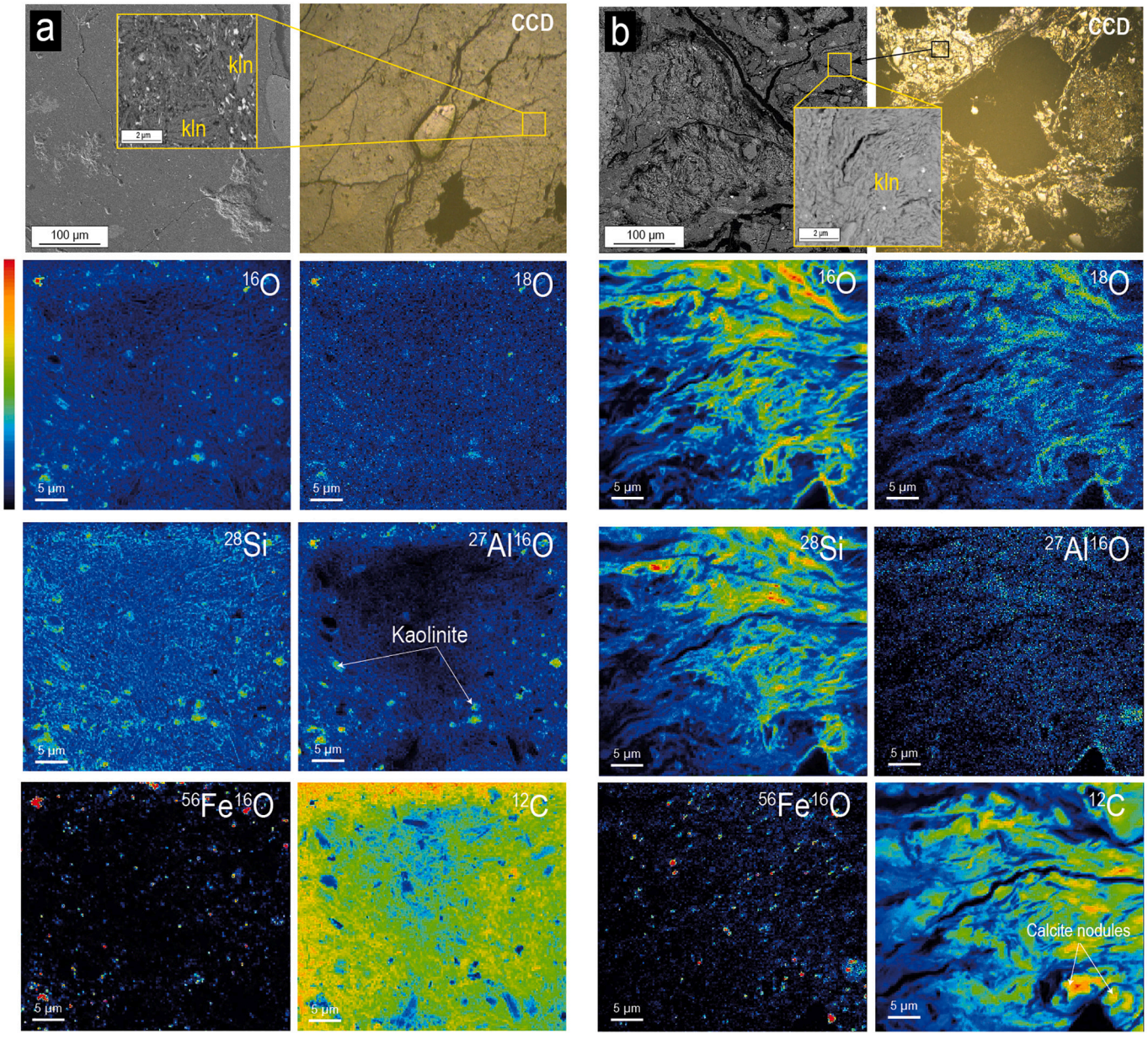

Fig. 3. 40 μm x 40 μm elemental maps obtained for the ions $^{16}O^-$, $^{18}O^-$, $^{28}Si^-$, $^{27}Al^{16}O^-$, $^{56}Fe^{16}O^-$ and $^{12}C^-$ in the thin sections of samples JO-1 (a) and ALC-4 (b). Images of the selected areas by FESEM and the same region observed in the CCD camera of the NanoSIMS are included to show the location of the maps in the sample. The images display kaolinite-rich areas ($^{16}O^-$, $^{18}O^-$, $^{28}Si^-$, $^{27}Al^{16}O^-$), iron-oxide-rich areas ($^{56}Fe^{16}O^-$) and areas with higher $^{12}C^-$ content, probably related to the resin or carbonates.

Clay minerals can be differentiated from the oxides and oxyhydroxides in the samples by their higher content in Si and Al ($^{28}Si^-$, $^{27}Al^{16}O^-$ maps in Figure 3a and b). The absence of K allowed to discard the presence of illitic phases. In addition, although the areas previously selected in the samples by FESEM were only enriched in kaolinite or smectite, the presence of Na also enabled the differentiation of smectite from kaolinite.

In some samples, the high image resolution also allows the outlines of kaolinite crystals to be identified (Figure 3a).

The topography of the surface plays an important role in the reproducibility and accuracy of the NanoSIMS measurements (Höschen et al., 2013; Thomen et al., 2014). When a rough, uneven sample surface is present, the impact of the primary ion beam in certain analysis zones may not be perpendicular, which results in different secondary ion yields depending on the angle of the beam and leads to artefacts in the image. Accordingly, the quality of the image is directly related with the polishing of the sample (Höschen et al., 2015).

However, thick polished sections have a high content of epoxy resin. The resin can capture atmospheric air and water during the embedding process, resulting in a degassing of the sample in the high vacuum of the analysis chamber. In this case, degassing led to deterioration of the high vacuum, in turn leading to lower secondary ion yields for the ions and thus lower-resolution elemental images. As pointed out above, this effect was partially compensated by using longer dwell times and higher Cs^+ currents, but still the results obtained in thick polished sections were worse than in thin sections. For this reason, the study focused in greater detail on the thin sections, where the low epoxy content (just a cover) produced more favourable vacuum conditions in the analysis chamber for elemental imaging and oxygen and hydrogen isotopic analyses.

The palaeosol samples used in this study showed varying degrees of consolidation. For example, sample JO-1 was better consolidated, so a good polishing could be achieved in the thin section. This is reflected in the NanoSIMS images obtained from this sample, where the resolution is high and kaolinite crystals can be clearly differentiated from the iron oxides and oxyhydroxides by their higher content in Si and Al ($^{28}Si^-$ and $^{27}Al^{16}O^-$ maps in Figure 3a).

In comparison, sample ALC-4 was poorly consolidated, and part of it was removed during the polishing of the thin section, giving rise to a more irregular surface, which clearly affects the quality of the elemental images (Figure 3b). The areas with little or no signal correspond to cracks or areas where sections of the sample were lost during polishing, as well as to areas that are deeper due to the irregular surface.

However, although it is more difficult to identify the outlines of kaolinite crystals due to these differences in polishing, certain areas with higher Si and Al and lower Fe content are differentiated ($^{28}Si^-$, $^{27}Al^{16}O^-$ and $^{56}Fe^{16}O^-$ maps in Figure 3b), allowing to carry out the isotopic analysis of kaolinite in sample ALC-4.

On the other hand, the intensely coloured areas in the $^{12}C^-$ maps are probably dominated by resin (Figure 3a), but some of the calcite nodules can also be differentiated (Figure 3b). The pre-sputtering of the sample surface of the sections increases the secondary ion yield by caesium implantation in the surface and can also remove the surface resin, but the pre-sputtering should be kept to the minimum possible in the thin section (just enough to reach a stable secondary ion signal) to prevent excessive consumption of the sample before analysis.

The relationship between the elements can be observed by overlying the elemental images, allowing the selection of areas for subsequent isotopic analyses (Figure 4). In the case of the palaeosol samples, $^{28}Si^-$ and $^{27}Al^{16}O^-$ maps show a perfect overlay in the areas rich in clay minerals, which are clearly differentiated from iron oxides ($^{56}Fe^{16}O^-$ maps). Figure 4 shows the overlaid $^{28}Si^-$, $^{27}Al^{16}O^-$ and $^{56}Fe^{16}O^-$ maps of 40 x 40 μm^2 in the thin sections of JO-1 and ALC-4, where the isotopic ratios of kaolinite were measured in 1 x 1 μm^2 areas (white squares in Figure 4).

4.2. NanoSIMS isotopic analysis

4.2.1. Oxygen and hydrogen isotopic analysis in the clay minerals

The average $\delta^{18}O$ and δD values relative to SMOW obtained for the neoformed clay minerals (kaolinite and smectite) in the thin sections

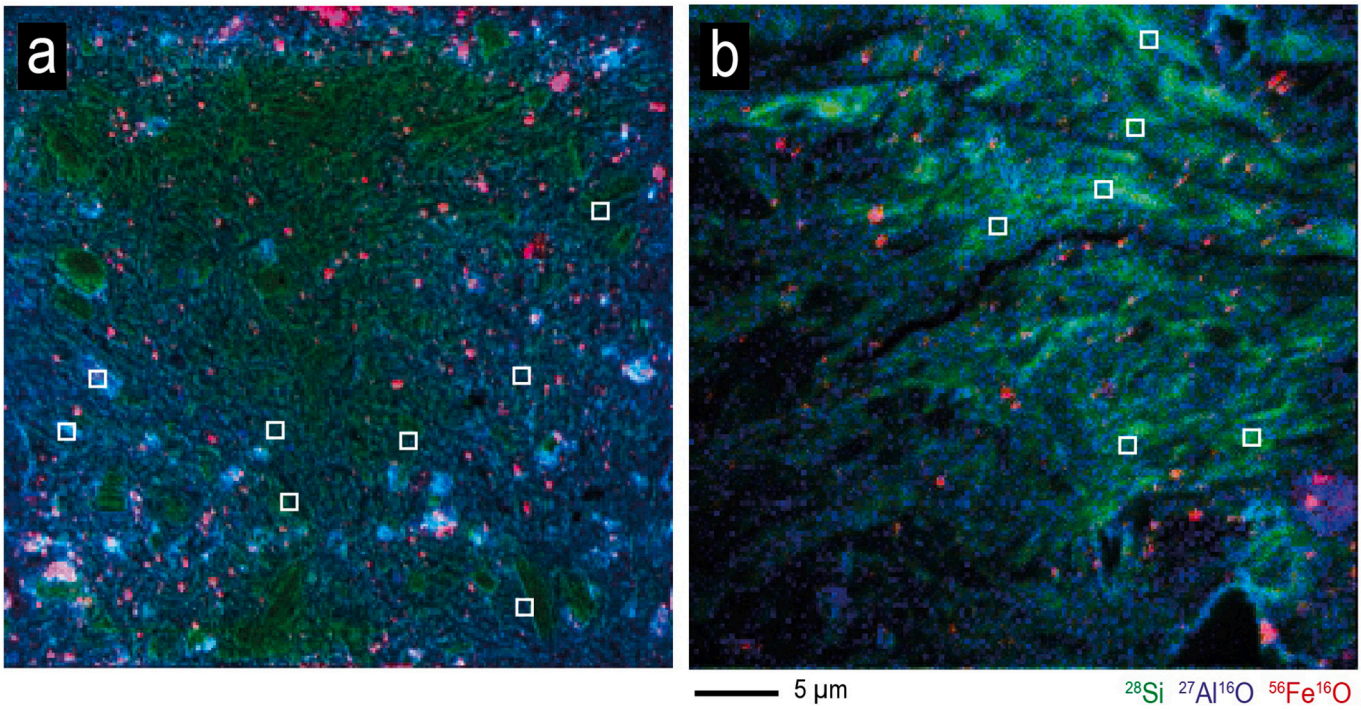

Fig. 4. Colour overlay of mapping of $^{28}Si^-$ (green), $^{27}Al^{16}O^-$ (blue) and $^{56}Fe^{16}O^-$ (red) in thin sections: a) colour overlay in sample JO-1, showing kaolinite outlines due to the good polishing; b) colour overlay in sample ALC-4, where kaolinite-rich areas (green and blue) can be differentiated from those with iron (red), but the bad polishing does not allow the kaolinite outlines to be distinguished. The white squares represent the 1 x 1 μm^2 points of the isotopic analyses.

from the ALC and JO profiles are represented in Figure 5. The detailed O and H isotope values for all the kaolinite and smectite analyses obtained in the thin sections and the thick polished sections can be found in Table 3.

Kaolinite from sample ALC-1 (bottom) displays average $\delta^{18}O$ and δD values of 18‰ (± 15‰) and -82‰ (± 36‰) respectively, which are similar than those for the kaolinite from sample ALC-4 (middle): $\delta^{18}O$ = 14‰ (± 4‰) and δD = -97‰ (± 37‰). The smectite from sample ALC-8 (top) shows significantly lower ratios than the kaolinites from the lower levels, with average $\delta^{18}O$ and δD values of 11‰ (± 6‰) and -180‰ (± 40‰), respectively (Figure 5a). Regarding the JO profile, the kaolinite from sample JO-1 (bottom) shows $\delta^{18}O$ and δD values of 81‰ (± 10‰) and 24‰ (± 42‰) respectively, which are significantly higher than those for the smectite from sample JO-5 (top): $\delta^{18}O_{SMOW}$ = 13 ‰ (± 14‰) and δD_{SMOW} = -167‰ (± 87‰) (Figure 5b). Comparing the two profiles, the kaolinite from the JO profile presents significantly higher $\delta^{18}O$ and δD values than the kaolinite from the ALC profile (samples ALC-1 and ALC-4). The smectite presents somewhat higher $\delta^{18}O$ and δD values in the JO profile (sample JO-5) than in the ALC profile (sample ALC-8), but this difference is much lower than that observed between the kaolinites from the two profiles. In any case, there is a decrease in the average oxygen and hydrogen isotope values of the clay minerals from bottom to top in both profiles (Table 3 and Figure 5).

The $^{18}O/^{16}O$ of kaolinite was also measured in the thick polished sections of samples ALC-1 and ALC-4, and the D/H ratio was also obtained in sample ALC-1. As in the thin sections, a decrease in the average $\delta^{18}O$ value of kaolinite from sample ALC-1, (34± 4‰), to sample ALC-4 (-17± 4‰), is observed in the thick polished sections. However, the $\delta^{18}O$ and δD values achieved by NanoSIMS for the thick polished sections are different from those obtained for the same samples in the thin sections. In sample ALC-1, the $\delta^{18}O$ of the kaolinite is higher in the thick polished section (34±4‰) than in the thin section (18±15‰). In sample ALC-4, by contrast, the $\delta^{18}O$ of the kaolinite is lower in the thick polished section (-17±4‰) than in the thin section (14±4‰). In addition, the δD value of the kaolinite in sample ALC-1, like the $\delta^{18}O$ value, is higher in the thick polished section (-64±43‰) than in the thin section (-82 ±36‰).

The uncertainties (expressed as standard deviations) for the isotope measures in the thin sections are in the range of ±4 to ±15‰ for the oxygen analyses and of ±36 to ±87‰ for the hydrogen analyses. Comparing with the thick polished sections, the standard deviation for the hydrogen measures in sample ALC-1 is similar in the thin section and the thick polished section (± 36‰ and ± 43‰, respectively), whereas for the oxygen analyses, the standard deviation is lower for the thick polished section measures (± 4‰), than for the measures in the thin section (± 15‰).

As previously mentioned, both analysis conditions consisted in spots of 1 x 1 μm^2 scanned with 32 x 32 pixels, during 270 measurements. However, a higher Cs^+ current was used in thick polished sections than in thin sections, 5.0 pA versus 2.0 pA Cs^+, and higher integration times in thick polished sections (1.5 min with a dwell time of 244 μs/pixel versus 1 min with 132 μs/pixel). These higher integration times could be the reason for the lower standard deviations obtained in the oxygen analyses from the thick polished sections (±4 ‰) compared to those from the thin sections (±4–18‰).

Nevertheless, despite the lower standard deviations obtained in the thick polished sections analyses, the differences in the $\delta^{18}O_{SMOW}$ and δD_{SMOW} compared with the thin sections could be related to their high

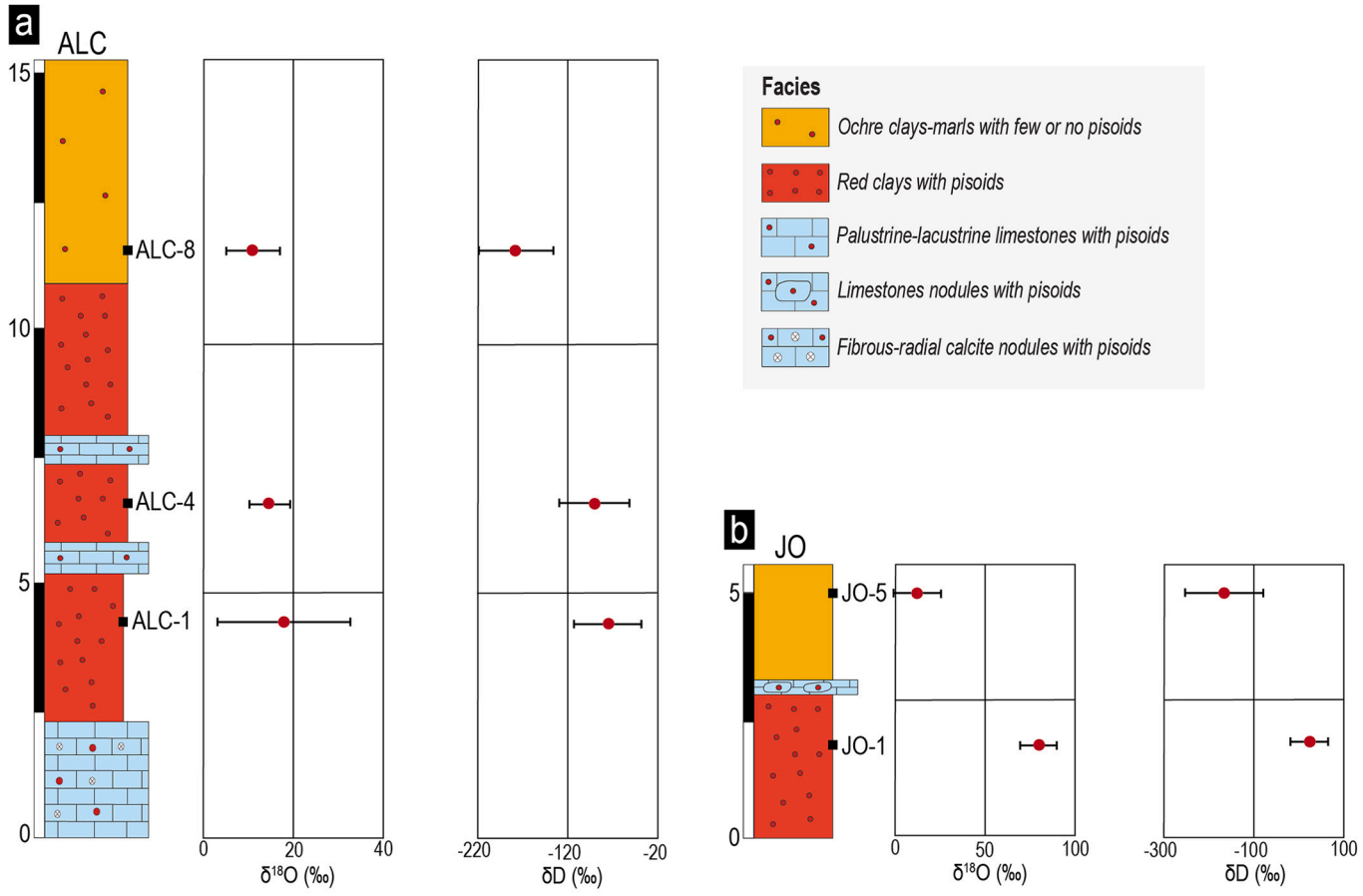

Fig. 5. Stratigraphic logs of the ALC (a) and JO (b) Lower Barremian continental profiles including the palaeosol levels (modified from Laita et al., 2020). The $\delta^{18}O$ and δD average values (with the standard deviations) obtained in each palaeosol sample are represented, showing a decrease from bottom to top in both profiles.

Table 3
$^{18}O/^{16}O$ and D/H and $\delta^{18}O$ and δD values obtained for the kaolinite and smectite in the palaeosol samples. SD=standard deviation.

Sample	$^{18}O/^{16}O$	D/H	$\delta^{18}O$ (‰)	δD (‰)	Sample	$^{18}O/^{16}O$	D/H	$\delta^{18}O$ (‰)	δD (‰)	Sample	$^{18}O/^{16}O$	D/H	$\delta^{18}O$ (‰)	δD (‰)	Sample	$^{18}O/^{16}O$	$\delta^{18}O$ (‰)
ALC-1	$2.05x10^{-3}$	$1.38x10^{-4}$	29	-129	ALC-1	$2.07x10^{-3}$	$1.47x10^{-4}$	37	-72	ALC-4	$2.01x10^{-3}$	1.45E-04	8	-81	ALC-4	$1.96x10^{-3}$	-16
Kaolinite	$2.07x10^{-3}$	$1.47x10^{-4}$	38	-73	Kaolinite	$2.06x10^{-3}$	$1.55x10^{-4}$	33	-17	Kaolinite	$2.03x10^{-3}$	1.31E-04	19	-169	Kaolinite	$1.96x10^{-3}$	-16
(Thin	$2.06x10^{-3}$	$1.44x10^{-4}$	36	-91	(Thick	$2.05x10^{-3}$	$1.56x10^{-4}$	27	-13	(Thin	$2.03x10^{-3}$	1.43E-04	18	-97	(Thick	$1.95x10^{-3}$	-23
section)	$2.07x10^{-3}$	$1.43x10^{-4}$	36	-93	polished	$2.05x10^{-3}$	$1.53x10^{-4}$	29	-34	section)	$2.02x10^{-3}$	1.45E-04	16	-80	polished	$1.96x10^{-3}$	-17
Analytical	$2.06x10^{-3}$	$1.40x10^{-4}$	35	-113	section)	$2.07x10^{-3}$	$1.44x10^{-4}$	36	-88	Analytical	$2.02x10^{-3}$	1.49E-04	16	-57	section)	$1.97x10^{-3}$	-10
session: 1	$2.02x10^{-3}$	$1.37x10^{-4}$	11	-132	Analytical	$2.07x10^{-3}$	$1.40x10^{-4}$	39	-116	session: 3	$2.01x10^{-3}$	1.47E-04	11	-71	Analytical	$1.95x10^{-3}$	-22
	$2.03x10^{-3}$	$1.47x10^{-4}$	19	-69	session: 2	$2.06x10^{-3}$	$1.41x10^{-4}$	31	-107		-	1.46E-04	-	-79	session: 3	$1.96x10^{-3}$	-19
	$2.01x10^{-3}$	$1.52x10^{-4}$	8	-39		$2.06x10^{-3}$	-	36	-		-	1.34E-04	-	-153		$1.96x10^{-3}$	-14
	$2.00x10^{-3}$	$1.49x10^{-4}$	1	-57		$2.07x10^{-3}$	-	36	-		-	1.49E-04	-	-57		$1.96x10^{-3}$	-17
	$2.00x10^{-3}$	$1.53x10^{-4}$	1	-29		-	-	-	-		-	1.43E-04	-	-93		$1.96x10^{-3}$	-15
	$2.03x10^{-3}$	-	20	-		-	-	-	-		-	1.38E-04	-	-126		$1.96x10^{-3}$	-15
	$2.01x10^{-3}$	-	6	-		-	-	-	-		-	-	-	-		-	-
	$2.00x10^{-3}$	-	1	-		-	-	-	-		-	-	-	-		-	-
	$2.01x10^{-3}$	-	6	-		-	-	-	-		-	-	-	-		-	-
Average	$2.03x10^{-3}$	$1.45x10^{-4}$	18	-82		$2.06x10^{-3}$	$1.48x10^{-4}$	34	-64		$2.02x10^{-3}$	$1.43x10^{-4}$-04	14	-97		**$1.96x10^{-3}$**	**-17**
SD	($\pm2.91x10^{-5}$)	($\pm5.64x10^{-6}$)	($\pm$15)	($\pm$36)		($\pm8.45x10^{-6}$)	($\pm6.75x10^{-6}$)	($\pm$4)	($\pm$43)		($\pm8.95x10^{-6}$)	($\pm5.86x10^{-6}$)	($\pm$4)	($\pm$37)		**($\pm7.59x10^{-6}$)**	**($\pm$4)**

Sample	$^{18}O/^{16}O$	D/H	$\delta^{18}O$ (‰)	δD (‰)	Sample	$^{18}O/^{16}O$	D/H	$\delta^{18}O$ (‰)	δD (‰)	Sample	$^{18}O/^{16}O$	D/H	$\delta^{18}O$ (‰)	δD (‰)
ALC-8	$2.00x10^{-3}$	$1.32x10^{-4}$	3	-164	JO-1	$2.17x10^{-3}$	$1.65x10^{-4}$	87	45	JO-5	$2.03x10^{-3}$	$1.35x10^{-4}$	17	-145.7
Smectite	$2.00x10^{-3}$	$1.20x10^{-4}$	4	-240	Kaolinite	$2.14x10^{-3}$	$1.61x10^{-4}$	72	16	Smectite	$2.00x10^{-3}$	$1.28x10^{-4}$	5	-187.0
(Thin	$2.01x10^{-3}$	$1.29x10^{-4}$	10	-183	(Thin	$2.13x10^{-3}$	$1.71x10^{-4}$	70	81	(Thin	$2.06x10^{-3}$	$1.33x10^{-4}$	32	-156.6
section)	$2.02x10^{-3}$	$1.28x10^{-4}$	11	-187	section)	$2.17x10^{-3}$	$1.71x10^{-4}$	86	82	section)	$2.06x10^{-3}$	$1.39x10^{-4}$	32	-118.2
Analytical	$2.03x10^{-3}$	$1.38x10^{-4}$	18	-126	Analytical	$2.13x10^{-3}$	$1.68x10^{-4}$	69	65	Analytical	$2.04x10^{-3}$	$1.35x10^{-4}$	23	-144.5
session: 4	$2.03x10^{-3}$	$1.27x10^{-4}$	17	-193	session: 3	$2.15x10^{-3}$	$1.57x10^{-4}$	78	-7	session: 4	$1.98x10^{-3}$	$1.34x10^{-4}$	-5	-151.9
and 5	$2.03x10^{-3}$	$1.39x10^{-4}$	18	-121	and 6	$2.16x10^{-3}$	$1.60x10^{-4}$	84	12	and 7	$2.03x10^{-3}$	$1.38x10^{-4}$	17	-123.7
	$2.01x10^{-3}$	$1.23x10^{-4}$	8	-224		$2.19x10^{-3}$	$1.70x10^{-4}$	99	78		$2.04x10^{-3}$	$1.23x10^{-4}$	23	-220.1
	$2.00x10^{-3}$	$1.30x10^{-4}$	5	-180		-	$1.55x10^{-4}$	-	-22		$2.04x10^{-3}$	$1.35x10^{-4}$	24	-146.8
	-	-	-	-		-	$1.55x10^{-4}$	-	-18		$1.99x10^{-3}$	$1.23x10^{-4}$	-4	-224.1
	-	-	-	-		-	$1.65x10^{-4}$	-	43		$2.00x10^{-3}$	$1.23x10^{-4}$	1	-218.8
	-	-	-	-		-	$1.52x10^{-4}$	-	-37		$1.99x10^{-3}$	-	1	-
	-	-	-	-		-	$1.58x10^{-4}$	-	-2		$1.99x10^{-3}$	-	-3	-
	-	-	-	-		-	$1.68x10^{-4}$	-	61		-	-	-	-
	-	-	-	-		-	$1.65x10^{-4}$	-	47		-	-	-	-
	-	-	-	-		-	$1.58x10^{-4}$	-	-1		-	-	-	-
	-	-	-	-		-	$1.52x10^{-4}$	-	-41		-	-	-	-
Average	$2.01x10^{-3}$	$1.30x10^{-4}$	11	-180		$2.15x10^{-3}$	$1.62x10^{-4}$	81	24		$2.02x10^{-3}$	$1.32x10^{-4}$	13	-167
SD	($\pm1.20x10^{-5}$)	($\pm6.67x10^{-6}$)	($\pm$6)	($\pm$40)		($\pm3.42x10^{-5}$)	($\pm6.65x10^{-6}$)	($\pm$10)	($\pm$42)		($\pm2.79x10^{-5}$)	($\pm6.14x10^{-6}$)	($\pm$14)	($\pm$87)

content in epoxy resin. As pointed out above, the high content of epoxy resin in the thick polished sections can result in a degassing of the sample, affecting the high vacuum (Aboura and Moore, 2021) and thus leading to lower secondary ion yields and resulting in poor-quality elemental mapping. Furthermore, the resin can also produce interference in the H and O ratios (Stadermann et al., 2005). Due to the poor-quality imaging, therefore, the ratios measured in the thick polished section may be altered not only by the resin but also by other mineral phases present in the samples (e.g., Fe oxides, quartz or carbonates).

4.2.2. Palaeoclimatic interpretation from the preliminary isotopic results

The average of the $\delta^{18}O_{SMOW}$ and δD_{SMOW} values obtained in the ALC and JO profiles, showed a decrease from kaolinite to the smectite in the studied palaeosol, despite the somewhat high standard deviations in some of the analyses, this decrease could be reflecting an enrichment in the light isotopes ^{16}O and ^{1}H towards the top of the profiles, may be due to a change in the palaeoclimatic conditions.

Comparing both profiles, kaolinite from sample JO-1 presented higher $\delta^{18}O_{SMOW}$ and δD_{SMOW} (81±10‰ and 24±42‰, respectively) than those of the kaolinites from the ALC profile (ALC-1: $\delta^{18}O$=18±15‰ and δD=-82±36‰; ALC-4: $\delta^{18}O$=14±4‰ and δD=-97±37‰) and the standard ($\delta^{18}O$=19.8‰ and δD=-62.4‰). This may indicate that this kaolinite underwent some process after its origin during soil formation (e.g., diagenesis), altering its original isotopic signature. This is also supported by the mineralogical data reported by Laita et al. (2020), since this kaolinite displays larger crystals sizes than that of the ALC profile (see Figure 1) and the average full width at half maximum (FWHM) value of the 001 reflections is lower (JO kaolinite=0.4; ALC kaolinite=0.5), indicating that is more crystalline. The characteristics of this kaolinite are compatible with a recrystallization process. For this reason, the $\delta^{18}O$ and δD values of this kaolinite are not used for the palaeoclimatic deductions.

On the other hand, as the isotope values obtained by NanoSIMS in the thin sections are more consistent than those from the thick polished sections, the average $\delta^{18}O$ and δD values from thin sections relative to SMOW for kaolinites (samples ALC-1 and ALC-4) and smectites (samples ALC-8 and JO-5) are plotted on a $\delta^{18}O$-δD diagram (Figure 6). The isotopic values of kaolinite from sample JO-1 are not included in Figure 6 since as just explained, they were discarded for the palaeoclimatic interpretation.

The average $\delta^{18}O_{SMOW}$ and δD_{SMOW} values of the neoformed kaolinite and smectite are within the range commonly reported for these minerals (Delgado and Reyes, 1996; Savin and Hsieh, 1998; Gilg et al., 2003; Fernández-Caliani et al., 2010; Mix and Chamberlain, 2014; Clauer et al., 2015; He et al., 2019).

The average kaolinite isotopic of neoformed kaolinites in samples ALC-1 and ALC-4 compositions depict two points on the kaolinite line calculated at 20°C (Sheppard and Gilg, 1996) (Figure 6a), whereas the average isotopic compositions of neoformed smectites un samples ALC-8 and JO-5 are included between the smectite lines at 30 and 0°C reported by Mix and Chamberlain (2014) (Figure 6b).

Previous investigations have indicated that Mesozoic kaolinites that formed in different environments preserved their original $^{18}O/^{16}O$ and D/H ratios (Savin and Epstein, 1970; Lawrence and Taylor, 1972 Sheppard, 1977).

As the kaolinite and smectite from the studied lower Barremian palaeosols are neoformed phases (Laita et al., 2020), they may have formed in equilibrium with the environment, and their isotopic composition would thus depend on that of the meteoric water from which they crystallized (Savin and Epstein, 1970; Delgado and Reyes, 1996; Sheppard and Gilg, 1996).

The isotopic composition and temperature of the meteoric water from which the kaolinite and smectite crystallized can thus be estimated by combining the following equations:

[1] The meteoric-water equation $\delta D = 8\ \delta^{18}O + 10$ (Craig, 1961)

[2] The equations relating the isotopic fractionation of oxygen to temperature in the kaolinite-water or smectite-water system:

[2.1] $10^3 \ln \alpha_{k\text{-}w} = 2.76 \times 10^6 T^{-2} - 6.75$ for kaolinite (Sheppard and Gilg, 1996)

[2.2] $10^3 \ln \alpha_{sm\text{-}w} = 2.55 \times 10^6 T^{-2} - 4.05$ for smectite (Sheppard and Gilg, 1996)

[3] The equations relating the isotopic fractionation of hydrogen to temperature in the kaolinite-water or smectite-water system:

[3.1] $1000 \ln \alpha_{k\text{-}w} = -2.2 \times 10^6 T^{-2} - 7.7$ for kaolinite (Sheppard and Gilg, 1996)

[3.2] $1000 \ln \alpha_{sm\text{-}w} = -7.5 \times 10^6 T^{-2} + 27.37$ for smectite (Capuano, 1992)

Applying these equations, the estimated crystallization temperatures

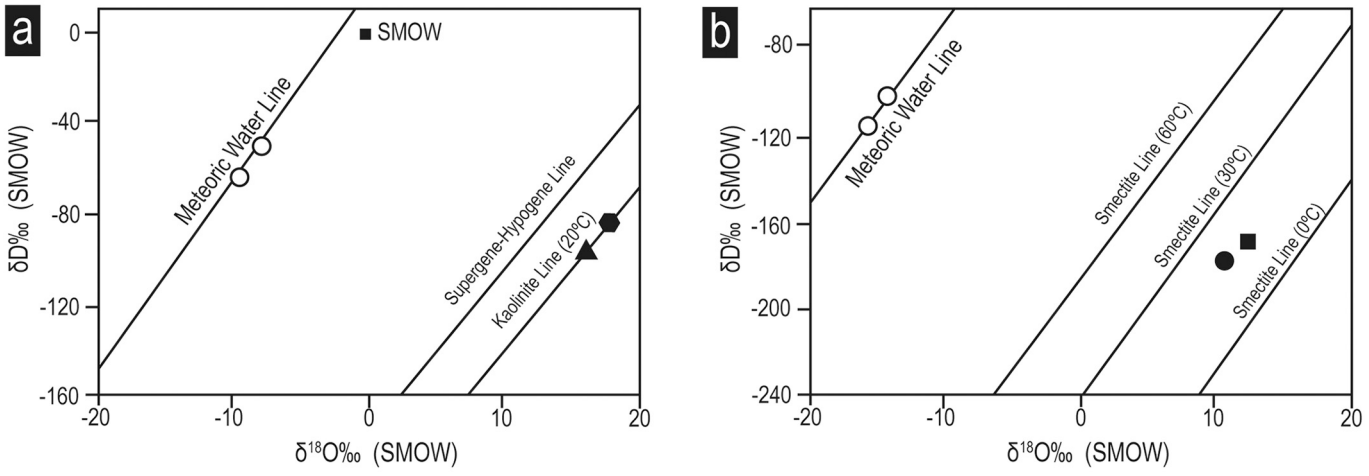

Fig. 6. a) Average $\delta^{18}O_{SMOW}$ and δD_{SMOW} values of kaolinite included in the bottom (black hexagon) (standard deviation: $\delta^{18}O$=±15‰ and δD=± 36‰) and middle levels (black triangle) (standard deviation: $\delta^{18}O$=±4‰ and δD=±37‰) of the ALC profile. The supergene-hypogene line (Sheppard et al., 1969), the kaolinite weathering line at 20°C (Sheppard and Gilg, 1996), the meteoric water line (Craig, 1961), and the isotopic composition of modern ocean water (SMOW) are given as references. The open circles correspond to the oxygen and hydrogen isotopic composition of the water with which kaolinite formed in equilibrium at 21-22°C (same standard deviation that the kaolinite analyses); b) Average $\delta^{18}O_{SMOW}$ and δD_{SMOW} values of smectite included in the top level of the ALC profile (black circle) (standard deviation: $\delta^{18}O$=±6‰ and δD=±40‰) and the top level of the JO profile (black square) (standard deviation: $\delta^{18}O$=±14‰ and δD=±87‰). The smectite lines at 0°C, 30°C, 60°C (Mix and Chamberlain, 2014) and the meteoric water line (Craig, 1961) are given as references. The open circles correspond to the oxygen and hydrogen isotopic composition of the water with which smectite formed in equilibrium at 16-17°C (same standard deviation that the smectite analyses).

are 21–22°C for the kaolinites of samples ALC-1 and ALC-4, whereas the estimated crystallization temperatures for the smectite in samples JO-5 and ALC-8 are 16–17°C.

The $\delta^{18}O$ and δD values inferred for the waters are $\delta^{18}O_{SMOW}$ = -7.5‰ and δD_{SMOW} = -48.7‰ for the kaolinite from sample ALC-1 and $\delta^{18}O_{SMOW}$ = -9.2‰ and δD_{SMOW} = -62.6‰ for the kaolinite from sample ALC-4. The $\delta^{18}O$ and δD values for the water of smectites are $\delta^{18}O_{SMOW}$ = -15.6‰ and δD_{SMOW} = -118.4‰ and $\delta^{18}O_{SMOW}$ = -13.4‰ and δD_{SMOW} = -106.0‰ for the smectites in samples ALC-8 and JO-5, respectively. All the calculated $\delta^{18}O$ and δD values for the waters plot on the meteoric water line (see Figure 6). The standard deviations of these values are in the same range as those of the $\delta^{18}O$ and δD values for kaolinite and smectite (see the 4.2.1 section).

Lower $^{18}O/^{16}O$ ratios in kaolinites suggest colder intervals in the past (Giral-Kacmarcík et al., 1998), and the $\delta^{18}O$ and δD values of meteoric water decrease with the decrease in temperature, which should be reflected in the clays formed from this water (Savin and Hsieh, 1998).

Laita et al. (2020) described a decrease in the neoformed kaolinite and oxides and oxyhydroxides content, along with an increase in the content of neoformed smectite and detrital quartz and illite, from the bottom to the top of the lateritic profiles studied here. These changes reflect less intense chemical weathering towards the top of the profiles, perhaps associated with a change from warm and humid to generally colder and drier conditions.

The average $\delta^{18}O$ and δD values obtained by NanoSIMS for the neoformed kaolinite and smectite in the studied palaeosol samples agree with the change in climatic conditions from the bottom to the top of the lateritic profiles deduced by Laita et al. (2020) using mineralogical tools. The temperature estimated for the meteoric water also support this hypothesis, pointing out to a possible decrease from 21–22 to 16–17°C during the early Barremian in the studied area.

4.3. Application of NanoSIMS in palaeoclimatic studies involving nanometer-sized clay minerals

NanoSIMS reported averages of $^{18}O/^{16}O$ ratio values for the kaolinite standard from $1.97x10^{-3}$ ($\pm 4.64x10^{-5}$) to $2.01x10^{-3}$ ($\pm 8.38x10^{-5}$) in the different analytical sessions and averages of D/H values from $1.44x10^{-4}$ ($\pm 2.52x10^{-6}$) to $1.55\ x10^{-4}$ ($\pm 2.49x10^{-5}$). In the same way, the averages $^{18}O/^{16}O$ ratios obtained by NanoSIMS for the smectite standard in the different analytical sessions ranged from $2.00x10^{-3}$ ($\pm 6.40x10^{-5}$) to $2.04x10^{-3}$ ($\pm 3.83x10^{-5}$) and the averages D/H ratios reported for this mineral ranged from $1.21x10^{-4}$ ($\pm 4.52x10^{-6}$) to $1.46x10^{-4}$ ($\pm 3.34x10^{-5}$). These values are close to those of the reference laboratory ($^{18}O/^{16}O$=$2.3x10^{-3}$ for kaolinite and smectite; D/H=$1.48x10^{-4}$ for kaolinite and $1.45x10^{-4}$ for smectite).

Although the standard deviations are in the range of ±4–15‰ for $\delta^{18}O$ and ±36–87‰ for δD, the average $\delta^{18}O_{SMOW}$ and δD_{SMOW} obtained by NanoSIMS for the neoformed kaolinite and smectite in the thin sections are within the range of values reported for these minerals in the literature.

The uncertainties of the preliminary hydrogen measures of this study are in the range reported by other authors in hydrogen analysis by NanoSIMS of samples containing hydrous silicates. For example, Barnes et al. (2014) analysed 4 x 4 μm^2 to 10 x 10 μm^2 areas in norite samples containing apatite crystals (with low H contents), reporting δD_{SMOW} values for these minerals of -281±49‰ or -27±98‰, and Lévy et al. (2019) obtained an overall uncertainty including reproducibility of 20‰ and ~50‰ relative to the Standard Mean Ocean Water reference on bulk FIB sections and at the 1.5 μm scale respectively when imaging D/H ratio in amphiboles.

On the other hand, lower uncertainties have been previously reported in the $\delta^{18}O$ values obtained from the analysis of 5 x 5 μm^2 areas in melilites included in chondrites (±3‰) or carbonates (±2.3‰) analysed by NanoSIMS (Ito and Messenger, 2008; Bojanowski et al., 2015).

Considering that the spots used for the analysis in the present work are smaller (1 x 1 μm^2) than the used in the previous studies mentioned (4 x 4 μm^2 to 10 x 10 μm^2), the obtained standard deviations for the O and H measurements are the expected for NanoSIMS analysis.

The results reported in the present study indicates that the technique shows promise. The high spatial resolution of NanoSIMS allowed us to obtain elemental images with enough quality for differentiating the neoformed kaolinite and smectite from the rest of the minerals present in the palaeosols samples (e.g., Fe oxides and oxyhydroxides and carbonates). This is a great advantage compared to traditional spectrometry.

In addition, the preliminary isotopic results showed a decrease in the average $\delta^{18}O$ and δD values from kaolinite of the bottom part to smectite of the top of the studied profiles, as well as a possible decrease in the temperature estimated for the formation of these minerals. On the other hand, the oxygen and hydrogen isotopic analysis by NanoSIMS also allowed neoformed kaolinites (formed during soil development) to be discriminated from those recrystallized during diagenesis (kaolinite from JO-1 sample).

However, it has also been pointed out that sample preparation plays an important role in the isotopic analysis by NanoSIMS, since the topography of the sample infers in the reproducibility and accuracy of the analysis and the thickness of the sample affects to the dwell time. In our case, for thin sections (30 μm thick) the dwell time had to be shorter than in the thick polished sections to not consume the sample and this could affect the precision of the analyses. As previously discussed, higher Cs^+ current and longer integration times could improve the uncertainties obtained in this preliminary study.

For this reason, future studies with thicker polished samples and lower epoxy resin content could be of interest to test if lower uncertainties can be achieved.

5. Conclusions

This study shows that, with suitable calibration using pure isotopic standards and appropriate sample preparation, NanoSIMS can be useful in the isotopic study of nanometre-sized clay minerals.

The high spatial resolution and accuracy of NanoSIMS allowed the elemental mapping and analysis of the oxygen and hydrogen isotopic compositions of nanometre-sized clay minerals from early Barremian polymineralic palaeosol samples within a complex matrix, where conventional spectrometry would have only provided average isotopic ratios of a mixture of several mineral phases.

The capacity of NanoSIMS to generate an elemental image of the sample surface permitted the precise localization of the minerals of interest. By the same token, the high spatial resolution enabled the measurement of the isotopic ratios in selected positions within the samples, excluding undesired mineral phases.

Two common sample preparation techniques in the geological sciences were tested. We showed that in the case of palaeosol samples, thin sections are better suited for NanoSIMS analysis than thick polished sections due to their lower resin content, even though a special in-house fabricated holder is required to introduce the thin sections into the NanoSIMS analysis chamber. However, the thickness of the thin section must be considered, since very thin samples can be consumed quickly and do not permit long dwell times, which can give place to greater uncertainty in the analyses.

The uncertainties of the isotopic measures are mainly due to the topography and the thickness of the sample, which prevented longer analysis times and that could be reduced with a more adequate sample preparation. Nevertheless, the average of the obtained preliminary results shows that oxygen and hydrogen isotopic values obtained by NanoSIMS allow populations of clay minerals formed under different conditions to be discriminated, since in this study neoformed and diagenetic kaolinites are differentiated.

There is a decrease in the average $\delta^{18}O_{SMOW}$ and δD_{SMOW} values of the neoformed kaolinite and smectite towards the top of the palaeosol profiles, reflecting a change in the climatic conditions.

These values indicate formation in a weathering environment at Earth-surface temperatures and the estimated average temperature formation for the clay minerals reflects a possible decrease from the kaolinite of the bottom lateritic levels (21–22 °C) to the smectite of the top lateritic levels (16–17°C) in the studied area during the early Barremian.

The results obtained from this study reflect, therefore, the potential of NanoSIMS for the acquisition of light isotope data (oxygen and hydrogen) in neoformed nanometer-sized clay minerals from palaeosols samples, opening up a novel path within this research field.

Declaration of Competing Interest

The authors declare that they have no known competing financial interests or personal relationships that could have appeared to influence the work reported in this paper.

Data availability

Data will be made available on request.

Acknowledgements

The work was supported by the European Regional Development Fund and the Government of Aragon [Aragosaurus Group: Geological Resources and Palaeoenvironments, grant number E18_20R] and the Spanish Ministry of Science, Innovation and Universities [grant numbers RTI2018-093419-B-100 and PID2021-123127OB-I00]. The authors acknowledge Anton Gusev of the SIAME laboratory (University of Pau and the Pays de l'Adour) for the fabrication of the sample holder. Authors would like to acknowledge the use of Servicio General de Apoyo a la Investigación-SAI, Universidad de Zaragoza and that of the Universidad de Salamanca (NUCLEUS). Elisa Laita is also grateful for a Government of Aragón grant for the development of her PhD. The authors would also like to thank the reviewers, whose comments and suggestions helped to improve the manuscript.

References

Aboura, Y., Moore, K.L., 2021. NanoSIMS analysis of hydrogen and deuterium in metallic alloys: Artefacts and best practice. Appl. Surf. Sci. 557, 149739 https://doi.org/10.1016/j.apsusc.2021.149736.

Agüi-Gonzalez, P., Jähne, S., Phan, N.T.N., 2019. SIMS imaging in neurobiology and cell biology. J. Anal. At. Spectrom. 34, 1355–1368. https://doi.org/10.1039/C9JA00118B.

Barnes, J., Tartèse, R., Anand, M., McCubbin, F.M., Franchi, I.A., Starkey, N.A., Russell, S.S., 2014. The origin of water in the primitive Moon as revealed by the lunar highlands samples. Earth Planet. Sci. Lett. 390, 244–252. https://doi.org/10.1016/j.epsl.2014.01.015.

Bauer, K.K., Vennemann, T.W., 2014. Analytical methods for the measurement of hydrogen isotope composition and water content in clay minerals by TC/EA. Chem. Geol. 363, 229–240. https://doi.org/10.1016/j.chemgeo.2013.10.039.

Bauluz, B., Yuste, A., Mayayo, M.J., Canudo, J.I., 2014. Early kaolinization ofdetrital Weald facies in the Galve Subbasin (Central Iberian Chain, north-east Spain) and its relationship to paleoclimate. Cretac. Res. 50, 214–227. https://doi.org/10.1016/j.cretres.2014.03.014.

Bird, M.I., Longstafee, F.J., Fyfe, W.S., Bildgen, P., 1992. Oxygen-isotope systematics in a multiphase weathering system in Haiti. Geochim. Cosmochim. Acta 56, 2831–2838. https://doi.org/10.1016/0016-7037(92)90362-M.

Blanc, W., Gullermier, C., Dussardier, B., 2012. Composition of nanoparticles in optical fibers by Secondary Ion Mass Spectrometry. Opt. Mater. Express. 2, 1504–1510. https://doi.org/10.1364/OME.2.001504.

Boiteau, R.M., Kukkadapu, R., Cliff, J.B., Smallwood, C.R., Kovarik, L., Wirth, M.G., Engelhard, M.H., Varga, T., Dohnalkova, A., Perea, D.E., Wietsma, T., Moran, J.J., Hofmockel, K.S., 2020. Calcareous organic matter coatings sequester siderophores in alkaline soils. Sci. Total Environ. 724, 138250 https://doi.org/10.1016/j.scitotenv.2020.138250.

Bojanowski, M.J., Bagiński, B., Guillermier, C., Franchi, I.A., 2015. Carbon and oxygen isotope analysis of hydrate-associated Oligocene authigenic carbonates using NanoSIMS and IRMS. Chem. Geol. 416, 51–64. https://doi.org/10.1016/j.chemgeo.2015.10.021.

Camuti, K.S., McGuire, P.T., 1999. Preparation of polished thin sections from poorly consolidated regolith and sediment materials. Sediment. Geol. 128, 171–178. https://doi.org/10.1016/S0037-0738(99)00073-1.

Capuano, R.M., 1992. The temperature dependence of hydrogen isotope fractionation between clay minerals and water: Evidence from a geopressured system. Geochim. Cosmochim. Acta 56, 2547–2554. https://doi.org/10.1016/0016-7037(92)90208-Z.

Chew, Y.V., Holmes, A.J., Cliff, J.B., 2014. Visualization of metabolic properties of bacterial cells using Nanoscale Secondary Ion Mass Spectrometry (NanoSIMS). In: Paulsen, I.T., Holmes, A.J. (Eds.), Environmental Microbiology Methods and Protocols. Humana Press, Totowa, pp. 133–146. https://doi.org/10.1007/978-1-62703-712-9_11.

Clauer, N., Fallick, A.E., Galán, E., Aparicio, P., Miras, A., Fernández-Caliani, J.C., Aubert, A., 2015. Stable isotope constraints on the origin of kaolin deposits from Variscan granitoids of Galicia (NW Spain). Chem. Geol. 417, 90–101. https://doi.org/10.1016/j.chemgeo.2015.09.022.

Craig, H., 1961. Standard for Reporting Concentrations of Deuterium and Oxygen-18 in Natural Waters. Science. 133, 1833–1834. https://doi.org/10.1126/science.133.3467.1833.

Delgado, A., Reyes, E., 1996. Oxygen and hydrogen isotope compositions in clay minerals: A potential single-mineral geothermometer. Geochim. Cosmochim. Acta 60, 4285–4289. https://doi.org/10.1016/S0016-7037(96)00260-8.

Dhillon, S.K., Dhillon, K.S., 1991. Characterisation of potassium in red (alfisols), black (vertisols) and alluvial (inceptisols and entisols) soils of India using electro-ultrafiltration. Geoderma 50, 185–196. https://doi.org/10.1016/0016-7061(91)90033-P.

Do Campo, M., Bauluz, B., del Papa, C., White, T., Yuste, A., Mayayo, M.J., 2018. Evidence of cyclic climatic changes recorded in clay mineral assemblages from a continental Paleocene-Eocene sequence, northwestern Argentina. Sediment. Geol. 368, 44–57. https://doi.org/10.1016/j.sedgeo.2018.03.007.

Ender, E., Subirana, M.A., Raab, A., Krupp, E.M., Schaumlöffel, D., Feldmann, J., 2019. Why is NanoSIMS elemental imaging of arsenic in seaweed (Laminaria digitata) important for understanding of arsenic biochemistry in addition to speciation information? J. Anal. At. Spectrom. 34, 2295–2302. https://doi.org/10.1039/C9JA00187E.

Fernández-Caliani, J.C., Galán, E., Aparicio, P., Miras, A., Márquez, M.G., 2010. Origin and geochemical evolution of the Nuevo Montecastelo kaolin deposit (Galicia, NW Spain). Appl. Clay Sci. 49, 91–97. https://doi.org/10.1016/j.clay.2010.06.006.

Gilg, H.A., Girard, J.P., Sheppard, S.M.F., 2004. Conventional and Less Conventional Techniques for Hydrogen and Oxygen Isotope Analysis of Clays, Associated Minerals and Pore Waters in Sediments and Soils. In: Groot, P.A. (Ed.), Handbook of Stable Isotope Analytical Techniques, 1. Elsevier, pp. 38–61.

Gilg, H.A., Weber, B., Kasbohm, J., Frei, R., 2003. Isotope geochemistry and origin of illite-smectite and kaolinite from the Seilitz and Kemmlitz kaolin deposits, Saxony, Germany. Clay Miner. 38, 95–112. https://doi.org/10.1180/0009855033810081.

Giral-Kacmarcík, S., Savin, S.M., Nahon, D.B., Girard, J.P., Lucas, Y., Abel, L.J., 1998. Oxygen isotope geochemistry of kaolinite in laterite-forming processes, Manaus, Amazonas, Brazil. Geochim. Cosmochim. Acta 62, 1865–1879. https://doi.org/10.1016/S0016-7037(98)00103-3.

Girard, J.P., Freyssinet, P., Chazot, G., 2000. Unraveling climatic changes from intra-profile variation in oxygen and hydrogen isotopic composition of goethite and kaolinite in laterites: an integrated study from Yaou, French Guiana. Geochim. Cosmochim. Acta 64, 409–426. https://doi.org/10.1016/S0016-7037(99)00299-9.

Girard, J.P., Freyssinet, P., Morillon, A.C., 2002. Oxygen isotope study of Cayenne duricrust paleosurfaces: implications for past climate and laterization processes over French Guiana. Chem. Geol. 30, 329–343. https://doi.org/10.1016/S0009-2541(02)00130-4.

He, S., Longstaffe, F.J., Zhou, Z., 2019. Stable isotopes of clay minerals from autoclave tests of oil sands: Implications for clay formation during steaming of Alberta Clearwater oil sands. Appl. Geochem. 104, 202–209. https://doi.org/10.1016/j.apgeochem.2019.04.001.

Hoefs, J., 1997. Stable isotope geochemistry. Springer, Berlin. https://doi.org/10.1007/978-3-319-19716-6, 201 pp.

Höschen, C., Mueller, C.W., Heister, K., Lugmeier, J., Kögel-Knabner, I., 2013. Application of NanoSIMS on Organo-Mineral Structures. NEA-RWM-CLAYCLUB–2013-1. Nuclear Energy Agency of the OECD (NEA).

Höschen, C., Höschen, T., Mueller, C.W., Lugmeier, J., Elgeti, S., Rennert, T., Kögel-Knabner, I., 2015. Novel sample preparation technique to improve spectromicroscopic analyses of micrometer-sized particles. Environ. Sci. Technol. 49, 9874–9880. https://doi.org/10.1021/acs.est.5b01636.

Hu, S., Lin, Y., Zhang, J., Hao, J., Feng, L., Xu, L., Yang, W., Yang, J., 2014. NanoSIMS analyses of apatite and melt inclusions in the GRV 020090 Martian meteorite: Hydrogen isotope evidence for recent past underground hydrothermal activity on Mars. Geochim. Cosmochim. Acta 140, 321–333. https://doi.org/10.1016/j.gca.2014.05.008.

Inagaki, T.M., Possinger, A.R., Grant, K.E., Schweizer, S.A., Mueller, C.W., Derry, L.A., Lehmann, J., Kögel-Knabner, I., 2020. Subsoil organo-mineral associations under contrasting climate conditions. Geochim. Cosmochim. Acta 270, 244–263. https://doi.org/10.1016/j.gca.2019.11.030.

Ito, M., Messenger, S., 2008. Isotopic imaging of refractory inclusions in meteorites with the NanoSIMS 50L. Appl. Surf. Sci. 255, 1446–1450. https://doi.org/10.1016/j.apsusc.2008.05.095.

Kilburn, M.R., Wacey, D., 2015. Nanoscale Secondary Ion Mass Spectrometry (NanoSIMS) as an analytical tool in the geosciences. In: Grice, K. (Ed.), Principles and Practice of Analytical Techniques in Geosciences. Royal Society of Chemistry, pp. 1–34. https://doi.org/10.1039/9781782625025-00001.

Kuligiewicz, A., Środoń, J., Liivamägi, S., 2021. Oxygen isotopic compositions of end-members in a multicomponent mixture: Ediacaran weathering material from the East European Craton. Geochim. Cosmochim. Acta 306, 245–262. https://doi.org/10.1016/j.gca.2021.04.013.

Laita, E., Bauluz, B., Aurell, M., Bádenas, B., Canudo, J.I., Yuste, A., 2020. A change from warm/humid to cold/dry climate conditions recorded in lower Barremian clay-dominated continental successions from the SE Iberian Chain (NE Spain). Sediment. Geol. 403, 105673 https://doi.org/10.1016/j.sedgeo.2020.105673.

Laita, E., Bauluz, B., Aurell, M., Bñadenas, B., Yuste, A., 2022. Weathering events recorded in uppermost Hauterivian–lower Barremian clay-dominated continental successions from the NW Iberian Range: climatic vs. tectonic controls. J. Iber. Geol. 1–19. https://doi.org/10.1007/s41513-021-00181-0.

Lawrence, J.R., Taylor, H.P., 1972. Hydrogen and oxygen isotope systematics in weathering profiles. Geochim. Cosmochim. Acta 36, 1377–1393. https://doi.org/10.1016/0016-7037(72)90068-3.

Lévy, D., Aléon, J., Aléon-toppani, A., Troadec, D., Duhamel, R., Gonzalez-cano, A., Bureau, H., Khodja, H., 2019. NanoSIMS imaging of D/H ratios on FIB sections. Anal. Chem. 91, 13763–13771. https://doi.org/10.1021/acs.analchem.9b03134.

Li, Q., Hu, X., Hao, J., Chen, W., Cai, P., Huang, Q., 2020. Characterization of Cu distribution in clay-sized soil aggregates by NanoSIMS and micro-XRF. *Chemosphere*. 249, 1–7. https://doi.org/10.1016/j.chemosphere.2020.126143.

Mack, G.H., James, W.C., Monger, H.C., 1993. Classification of paleosols. Geol. Soc. Am. Bull. 105, 129–136. https://doi.org/10.1130/0016-7606(1993)105<0129:COP>2.3.CO;2.

Malherbe, J., Penen, F., Isaure, M.P., Frank, J., Hause, G., Dobritzsch, D., Gontier, E., Horréard, F., Hillion, F., Schaumlöffel, D., 2016. A New Radio Frequency Plasma Oxygen Primary Ion Source on Nano Secondary Ion Mass Spectrometry for Improved Lateral Resolution and Detection of Electropositive Elements at Single Cell Level. Anal. Chem. 88, 7130–7136. https://doi.org/10.1021/acs.analchem.6b01153.

Mix, H., Chamberlain, C.P., 2014. Stable isotope records of hydrologic change and paleotemperature from smectite in Cenozoic western North America. Geochim. Cosmochim. Acta 141, 532–546. https://doi.org/10.1016/j.gca.2014.07.008.

Mosenfelder, J.K., Le Voyer, M., Rossman, G.R., Guan, Y., Bell, D.R., Asinow, P.D., Eiler, J.M., 2011. Analysis of hydrogen in olivine by SIMS: Evaluation of standards and protocol. Am. Mineral. 96, 1725–1741. https://doi.org/10.2138/am.2011.3810.

Mueller, C.W., Kölbl, A., Hoeschen, C., Hillion, F., Heister, K., Herrmann, A.M., Kögel-Knabner, I., 2012. Submicron scale imaging of soil organic matter dynamics using NanoSIMS–From single particles to intact aggregates. Org. Geochem. 42, 1476–1488. https://doi.org/10.1016/j.orggeochem.2011.06.003.

Piani, L., Remusat, L., Robert, F., 2012. Determination of the H Isotopic Composition of Individual Components in Fine-Scale Mixtures of Organic Matter and Phyllosilicates with the Nanoscale Secondary Ion Mass Spectrometry. Anal. Chem. 84, 10199–10206. https://doi.org/10.1021/ac301099u.

Piani, L., Robert, F., Remusat, L., 2015. Micron-scale D/H heterogeneity in chondrite matrices: A signature of the pristine solar system water? *Earth Planet*. Sci. Lett. 415, 154–164. https://doi.org/10.1016/j.epsl.2015.01.039.

Rennert, T., Händel, M., Höschen, C., Lugmeier, L., Steffens, M., Totsche, K.U., 2014. A NanoSIMS study on the distribution of soil organic matter, iron and manganese in a nodule from a Stagnosol. Eur. J. Soil Sci. 65, 684–692. https://doi.org/10.1111/ejss.12157.

Savin, S.M., Epstein, S., 1970. The oxygen and hydrogen isotope geochemistry of clay minerals. Geochim. Cosmochim. Acta 34, 25–42. https://doi.org/10.1016/0016-7037(70)90149-3.

Savin, S.M., Hsieh, J.C.C., 1998. The hydrogen and oxygen isotope geochemistry of pedogenic clay minerals: principles and theoretical background. Geoderma. 82, 227–253. https://doi.org/10.1016/S0016-7061(97)00103-1.

Sheldon, N.D., Tabor, N.J., 2009. Quantitative paleoenvironmental and paleoclimatic reconstruction using paleosols. Earth-Sci. Rev. 95, 1–52. https://doi.org/10.1016/j.earscirev.2009.03.004.

Sheppard, S.M.F., 1977. The Cornubian batholith, SW England: D/H and 18O/16O studies of kaolinite and other alteration minerals. J. Geol. Soc. 133, 573–591. https://doi.org/10.1144/gsjgs.133.6.0573.

Sheppard, S.M.F., Gilg, H.A., 1996. Stable isotope geochemistry of clay mienrals. Clay Miner. 31, 1–24. https://doi.org/10.1180/claymin.1996.031.1.01.

Sheppard, S.M.F., Nielsen, R.L., Taylor Jr, H.P., 1969. Oxygen and hydrogen isotope ratios of clay minerals from porphyry copper deposit. Econ. Geol. 64, 755–777. https://doi.org/10.2113/gsecongeo.64.7.755.

Stadermann, F.J., Croat, T.K., Bernatowicz, T.J., Amari, S., Messenger, S., Walker, R.M., Zinner, E., 2005. Supernova graphite in the NanoSIMS: Carbon, oxygen and titanium isotopic compositions of a spherule and its TiC sub-components. Geochim. Cosmochim. Acta 69, 177–188. https://doi.org/10.1016/j.gca.2004.06.017.

Subirana, M.A., Paton, L., Hall, J., Brownlow, A., Krupp, E.M., Feldmann, J., Schaumlöffel, D., 2021. Development of Mercury Analysis by NanoSIMS for the Localization of Mercury−Selenium Particles in Whale Liver. Anal. Chem. 93, 12733–12739. https://doi.org/10.1021/acs.analchem.1c02769.

Tabor, N.J., Montanez, I.P., Southard, R.J., 2002. Paleoenvironmental reconstruction from chemical and isotopic compositions of Permo-Pennsylvanian pedogenic minerals. Geochim. Cosmochim. Acta 66, 3093–3107. https://doi.org/10.1016/S0016-7037(02)00879-7.

Thomen, A., Robert, F., Remusat, L., 2014. Determination of the nitrogen abundance in organic materials by NanoSIMS quantitative imaging. J. Anal. At. Spectrom. 29, 512–519. https://doi.org/10.1039/c3ja50313e.

Vidal, A., Lenhart, T., Dignac, M.F., Biron, P., Höschen, C., Barthod, J., Vedere, C., Vaury, V., Bariac, T., Rumpel, C., 2020. Promoting plant growth and carbon transfer to soil with organic amendments produced with mineral additives. *Geoderma*. 374, 114454 https://doi.org/10.1016/j.geoderma.2020.114454.

Vogel, C., Mueller, C.W., Höschen, C., Buegger, F., Heister, K., Schulz, S., Schloter, M., Kögel-Knabner, I., 2014. Submicron structures provide preferential spots for carbon and nitrogen sequestration in soils. Nat. Commun. 5, 1–7. https://doi.org/10.1038/ncomms3947.

Wacey, D., Kilburn, M.R., Mcloughlin, N., Parnell, J., Stoakes, C.A., Grovenor, C.R.M., Brasier, M.D., 2008. Use of NanoSIMS in the search for early life on Earth: ambient inclusion trails in a c. 3400 Ma sandstone. J. Geol. Soc. Lond. 165, 43–53. https://doi.org/10.1144/0016-76492007-032.